



저작자표시-비영리-변경금지 2.0 대한민국

이용자는 아래의 조건을 따르는 경우에 한하여 자유롭게

- 이 저작물을 복제, 배포, 전송, 전시, 공연 및 방송할 수 있습니다.

다음과 같은 조건을 따라야 합니다:



저작자표시. 귀하는 원저작자를 표시하여야 합니다.



비영리. 귀하는 이 저작물을 영리 목적으로 이용할 수 없습니다.



변경금지. 귀하는 이 저작물을 개작, 변형 또는 가공할 수 없습니다.

- 귀하는, 이 저작물의 재이용이나 배포의 경우, 이 저작물에 적용된 이용허락조건을 명확하게 나타내어야 합니다.
- 저작권자로부터 별도의 허가를 받으면 이러한 조건들은 적용되지 않습니다.

저작권법에 따른 이용자의 권리는 위의 내용에 의하여 영향을 받지 않습니다.

이것은 [이용허락규약\(Legal Code\)](#)을 이해하기 쉽게 요약한 것입니다.

[Disclaimer](#)

Doctor of Philosophy

**DEVELOPMENT OF FACILE SYNTHESIS MEHTOD FOR
CHEMICALLY FUNCTIONALIZED GRAPHENE QUANTUM DOTS
AND THEIR APPLICATIONS.**

**THE GRADUATE SCHOOL
OF THE UNIVERSITY OF ULSAN**

**Department of Chemical Engineering
Tran, Van Tam**

**DEVELOPMENT OF FACILE SYNTHESIS MEHTOD FOR
CHEMICALLY FUNCTIONALIZED GRAPHENE QUANTUM DOTS
AND THEIR APPLICATIONS.**

Supervisor Won-Mook Choi

A Dissertation

Doctor of Philosophy in Chemical Engineering

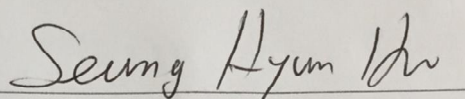
by

Tran, Van Tam

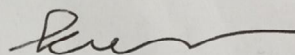
**Department of Chemical Engineering
Ulsan, Korea
December, 2017**

**Development of facile synthesis method for chemically
functionalized graphene quantum dots and their applications**

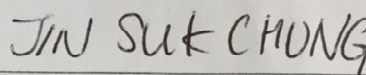
This certifies that the dissertation
of Tran Van Tam is approved



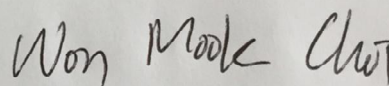
Committee Chair Prof Seung Hyun Hur



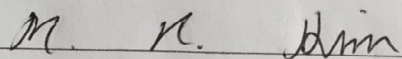
Committee Member Prof Sung Gu Kang



Committee Member Prof Jin Suk Chung



Committee Member Prof Won Mook Choi



Committee Member Prof Mun Ho Kim

Department of Chemical Engineering

Ulsan, Korea

November 2017

ACKNOWLEDGMENT

Firstly, I would like to express my sincerest gratitude to my supervisor, Professor Won-Mokk Choi for his kind help and support. During my study periods, Professor Choi has always given me good advices and supported me necessary things for my research. Without his great supports, I could not finish this dissertation as good as it. In addition, I am thankful to other professors in Department of Chemical Engineering for their dedication in experience and knowledge. Also, I would like to thank all members of Flexible and Nano Material Laboratory and other friends who kindly helped and shared their knowledge and living experience when I stayed in Korea. Finally, I deeply would like to thank my family for giving me great spiritual support. Thank to all, I had enough power to do my best to finish my Ph.D course in University of Ulsan, Korea.

Ulsan, December 2017

Tran, Van Tam

Publication list

- 1) One-pot synthesis of N-doped graphene quantum dots as fluorescent sensing platform for Fe³⁺ ion detection, Sensors and Actuators B.
- 2) Facile synthesis of cysteine-functionalized graphene quantum dots for a fluorescence probe for mercury ions, RSC Advances.
- 3) Ultraviolet light sensor based on graphene quantum dots/reduced graphene hybrid film, Sensor and Actuators A, accepted.
- 4) *Synthesis of B-doped graphene quantum dots as metal-free electrocatalyst for oxygen reduction, Journal of materials chemistry A.*
- 4) Facile synthesis of three-deminsional graphene/nickel oxide nanoparticles composites for high performance supercapacitor electrodes, Chemical Engineering Journal.
- 5) Three-dimensional hollow balls of graphene-polyaniline hybrids for supercapacitor applications, Chemical Engineering Journal.
- 6) Facile fabrication of thermally reduced graphene oxide-platium nanohybrids and their applications in catalytic reduction and dye-sensitized solar cells, RSC Advances.
- 7) Fabrication of sub-micrometer graphene ribbon using electronspun nanofiber, Journal of Materials Science.
- 8) Liquid-phase exfoliation of graphene in organic solvents with addition of naphthalene, Journal of Colloid and Interface Science.

ABSTRACT

This study has demonstrated the developing different types of functionalized graphene quantum dots (GQDs) by facile, green and cost effective bottom-up strategies. Characteristics of the as-prepared GQDs were investigated by several measurements, transmission electron microscope (TEM) , atomic force microscope, fluorescence , raman, XPS and FTIR spectroscopy. The modified GQDs possessed high quality of graphitic materials as well as interestingly tunable properties. The chemical functionalization significantly enhanced new disorder structures or functional groups on the surface of the GQDs, thus leading to effectively generate active sites or tailor electronic structures for specific purposes. Therefore the wide range applications have made based on unique properties of these functionalized GQDs. In particular, all these obtained GQDs have shown excellent practical potential, greatly promising an effective alternation for synthesizing and employing GQDs in reality.

TABLE OF CONTENTS

Contents

ACKNOWLEDGMENT	i
ABSTRACT	iii
LIST OF FIGURES	vi
LIST OF TABLES.....	viii
CHAPTER 1: Introduction	9
1.1 Graphene quantum dots	9
1.2 Properties of graphene quantum dots	10
1.3 Synthesis of graphene quantum dots	11
1.3.1 Top-down methods	12
1.3.1.1 Hydrothermal cutting.....	13
1.3.1.2 Solvothermal Cutting	13
1.3.1.3 Electrochemical Cutting.....	13
1.3.2 Bottom-up methods.....	14
1.4 Modification (functionalization) of graphene quantum dots	15
1.4.1 Pre-FabricationModification	15
1.4.2 Post-Fabrication Modification	16
1.5 Motivation	16
Reference.....	18
CHAPTER 2: One-pot synthesis of N-doped graphene quantum dots as a fluorescent sensing platform for Fe³⁺ ions detection.....	21
2.1 Introduction.....	21
2.2 Experiment	23
2.2.1 Synthesis of GQDs and N-GQDs	23
2.2.2 Characterizations	24
2.3 Results and discussion.....	25
2.4 Conclusion	33
Reference.....	33

CHAPTER 3: Ultraviolet light sensor based on graphene quantum dots/reduced graphene oxide hybrid film	37
3.1 Introduction.....	37
3.2 Experiment	38
3.2.1 Preparation of Graphene oxide	38
3.2.2 Synthesis of GQDs.....	39
3.2.3 Fabrication of GQDs/RGO UV sensor	39
3.2.4 Characterizations	40
3.3 Results and Discussion	41
3.4 Conclusion	49
Reference.....	50
CHAPTER 4: Facile synthesis of cysteine-functionalized graphene quantum dots for a fluorescence probe toward mercury ions	53
4.1 Introduction.....	53
4.2 Experiment	55
4.2.1 Synthesis of cys-GQDs	55
4.2.2 Characterizations	55
4.3 Results and discussions	56
4.4 Conclusion	68
Reference.....	68
CHAPTER 5: Synthesis of B-doped graphene quantum dots as metal-free electrocatalyst for oxygen reduction reaction	71
5.1 Introduction.....	71
5.2 Experiment	73
5.2.1 Synthesis of BGQD.....	73
5.2.2 Preparation of G-BGQD composites.....	73
5.2.3 Characterizations	74
5.2.4 Electrochemical measurements	75
5.2.5 Computational method	75
5.3 Results and discussion.....	76
5.4 Conclusion	88

Reference.....	89
CHAPTER 6: Conclusion.....	92

LIST OF FIGURES

Figure 1 Illustration of graphene and graphene quantum dots structures	10
Figure 2 Schematic diagram of two common methods for synthesis of GQDs	12
Figure 3 Synthesis illustration of GQDs and N-GQDs.....	25
Figure 4 Morphology and topology characteristics of N-GQDs	27
Figure 5 Chemical composition of GQDs and N-GQDs.....	29
Figure 6 Optical properties of GQDs and N-GQDs.....	31
Figure 7 Sensitivity and selectivity of N-GQDs for detecting Fe ³⁺	32
Figure 8 Schematic illustration for the fabrication of GQDs/RGO hybrids UV sensor	40
Figure 9 TEM and HRTEM images of GQDs.....	42
Figure 10 XPS spectra of the prepared GQDs.....	43
Figure 11 UV-Vis absorption spectra of GQDs.....	43
Figure 12 I-V curves of RGO and GQDs/RGO with and without UV	44
Figure 13 Sensitivity performance of GQDs/RGO	46
Figure 14 Photoluminescence spectra of RGO, GQDs and GQDs/RGO hybrids.....	48
Figure 15 Cathodic and anodic scan of GQDs	48
Figure 16 Schematic illustration of mechanism for enhanced performance of the GQDs/RGO hybrids UV sensor.....	49

Figure 17 Schematic illustration of the synthesis of cys-GQDs and its morphology	57
Figure 18 AFM images and the height distribution of cys-GQDs.....	58
Figure 19 Chemical composition of the cys-GQDs	60
Figure 20 FTIR and Raman spectroscopy of cys-GQDs.....	60
Figure 21 Optical properties of cys-GQDs.....	62
Figure 23 FTIR and PL decay spectroscopy of the cys-GQDs with and without Hg ²⁺	67
Figure 24 Schematic illustration for preparation of BGQD and G-BGQDs composites	74
Figure 25 TEM, HRTEM and FTIR spectrum of GQDs and BGQDs	77
Figure 26 Chemical composition of BGQDs	79
Figure 27 Morphology of G-BGQD composite.....	81
Figure 28 ORR Electrochemical performance of G-BGQD composite	82
Figure 29 Computationally optimized structures of lowest energy configurations of O ₂ adsorption on different B-C bond structures in BGQDs	85
Figure 30 Nyquist plots of different G-BGQD composites	86
Figure 31 Durability and methanol tolerance test of G-BGQDs test.....	87

LIST OF TABLES

Table 1 Quantum yield of GQDs and cys-GQDs	63
Table 2 Determination results of Hg ²⁺ in river water samples	65
Table 3 Chemical composition of boron in different BGQD samples.....	80

CHAPTER 1: Introduction

1.1 Graphene quantum dots

Fluorescent materials produce visible or invisible light as a result of incident light of a different wavelength. The effect ceases as soon as the source of excitement is removed. Semiconductor quantum dots (QDs) and small organic fluorescent dyes (OFDs) themselves as powerful fluorescent probes because of their high quantum yield and novel optical property. However, their more widely used applications are greatly limited by some of their disadvantages such as high toxicity, low biocompatibility, high cost and low chemical inertness. They show poor solubility/bio-availability in aqueous solution. Although the solubility can be improved by locating QDs into a shell (e.g., silica) or a stable surfactant layer, or by substituting polar groups on the periphery of OFDs, most of the modifications proceed in organic solvents. However, compared to conventional semiconductor quantum dots, graphene quantum dots (GQDs), which are superior in terms of chemical inertness, low cytotoxicity and excellent biocompatibility, have been found to be overwhelmingly superior to the traditional semiconductor [1-4].

Graphene quantum dots constitute a fascinating class of recently discovered nanocarbons that are small graphene fragments (Fig. 1), where electronic transport is confined in all three spatial dimensions. GQDs which comprise discrete, quasi-spherical nanoparticles typically have dimensions in the size range below 20 nm diameter. They possess several favorable attributes, such as resistance to photobleaching, size- and wavelength-dependent luminescence emission, ease of production and bioconjugation [5-6].

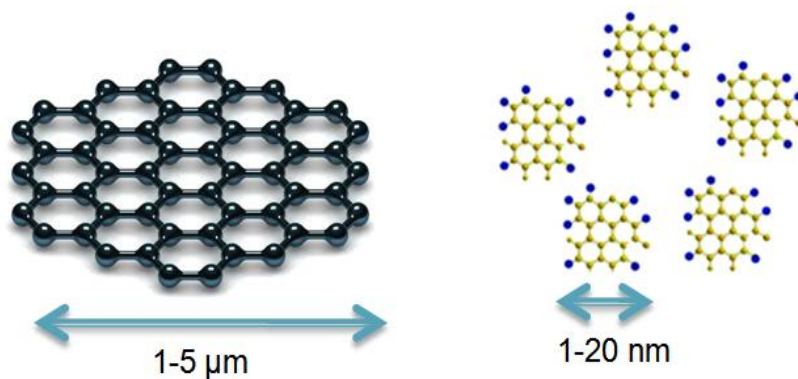


Figure 1 Illustration of graphene and graphene quantum dots structures.

In the early research on GQDs, tremendous effort was devoted to developing methods for the preparation of GQDs and exploring their properties. Their application in the analytical field has not been explored until very recently. Due to their novel properties, sensors based on GQDs can achieve a high level of performance. In this review, we primarily focus on sensors and analytical systems that utilize GQDs as a key component. The experimental and theoretical study of GQDs has followed the work on graphene very closely. GQDs have been fabricated by fragmentation or “cutting” of graphene sheets (top-down approach). In parallel, organic chemists synthesized large graphene-like molecules with well-defined molecular structure (bottom-up approach). The early work on GQDs was dominated by the investigation of their physical properties. More recently, GQDs have been chemically modified and used for the first time in applications in the area of sensing [7].

1.2 Properties of graphene quantum dots

Excitons in graphene have an infinite Bohr diameter. Thus, graphene fragments of any size will show quantum confinement effects. As a result, GQDs have a non-zero band gap and luminesce on excitation. This band gap is tunable by modifying the size and surface chemistry of the GQDs. Density functional theory (DFT) calculations have shown that the band gap of GQDs increases to approximately 2 eV in a GQD consisting of 20 aromatic rings

and 7 eV for benzene. Very little work has been done on the electronic properties of GQDs and apart from some early electrochemical measurements in the context of electrosynthesis, electrocatalysis, and sensing, there is very little known [8-11].

The absorption spectra of GQDs show a prominent peak at about 230 nm, which has been assigned to the $\pi \rightarrow \pi^*$ excitation of the π -bonds. Functional groups on the GQDs can introduce further absorption features and affect the photo luminescence (PL) (the so-called edge effect). The PL quantum yields reported for GQDs vary significantly. The main difference between GQD and semiconductor QD photoluminescence is that the PL bandwidth is much wider in GQDs and that their PL maximum shifts to the red and decreases with increasing excitation wavelength. It also has to be noted that the spectroscopic properties of GQDs may vary depending on the method of preparation and the functional groups at the edges of the particles.

One of the most attractive properties of GQDs is the fact that they are a carbon material and thus abundantly available (in principle), showing low toxicity, highly soluble in various solvents and can be equipped with functional groups at their edges. These properties make them much more desirable for many applications compared with inorganic semiconductor QDs. However, research on GQDs is still in an early stage and the full potential of this material has not yet been fathomed.

1.3 Synthesis of graphene quantum dots

The synthetic approaches towards GQDs fall into two broad categories: top-down and bottom-up methods. Top-down methods involve the decomposition and exfoliation of cheap, readily available bulk graphene-based materials, most commonly graphite, in harsh conditions. Such methods usually require multiple steps involving concentrated acids, strong oxidizing agents, and high temperatures. These methods lack precise control of the

morphology and size distribution of the particles produced. Bottom-up methods, however, involve the synthesis of quantum dots from polycyclic aromatic compound or other molecules with aromatic structures such as fullerenes. Although complex, these methods allow for excellent control of the properties of the final product [12].

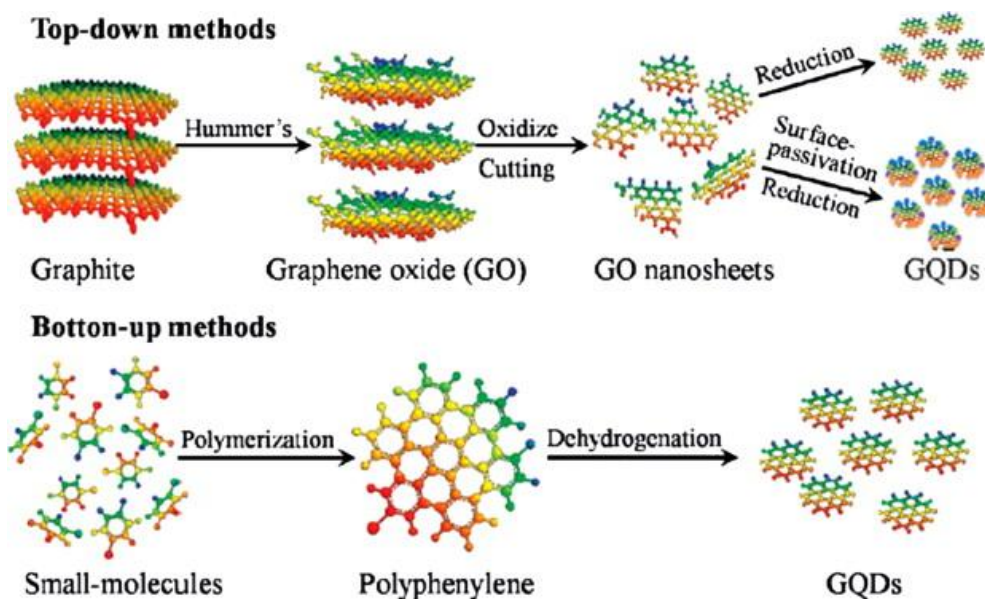


Figure 2 Schematic diagram of two common methods for synthesis of GQDs.

1.3.1 Top-down methods

The first step in many methods is the conversion of a graphite based starting material to graphite oxide sheets. Most commonly, a modified Hummers method is used. This method uses a mix of sulfuric acid, sodium nitrate, and potassium permanganate or similar reagents. The majority of top-down methods then differ in the ways they convert these GO sheets to quantum dots [13,14].

1.3.1.1 Hydrothermal cutting

The method involved several steps, namely, thermal reduction of graphene oxide to graphene sheets, oxidation of graphene sheets in acid media and hydrothermal reduction to afford the GQDs. Shown in figure. , the mechanism is proposed to explain how the graphene sheets are cut into quantum dots during the hydrothermal process based on what is known about the breakdown of carbon nanotubes into smaller tubes and nanoribbons in acid media. The oxidation step, in acidic conditions, creates epoxy groups that tend to form in a line along a carbon lattice causing a rupture of the C–C bonds. The epoxy chain is then further oxidized into epoxy pairs that are converted to more stable carbonyl pairs. It is these carbonyl groups that remain after the subsequent alkaline hydrothermal step making the GQDs dispersible in water. The linear defects can cause further break up during the hydrothermal reduction process where the oxygen atoms are removed [15].

1.3.1.2 Solvothermal Cutting

The GO was cut and reduced in one step using DMF as solvent and reducing agent. This was followed by column chromatography separation. In this way, GQDs with differing degrees of oxidation have been separated and therefore batches of particles with more defined photoluminescence were obtained [16].

1.3.1.3 Electrochemical Cutting

GQDs of 3–5 nm in size were produced through an electrochemical method that involved the breaking up of a graphene film that has been treated with oxygen plasma to increase hydrophilicity. The particles remained stable in water for several months.

The water-soluble GQDs in high yield and with good size uniformity were prepared by electrochemically exfoliating graphite and by reducing the resulting nano-scale GQDs with hydrazine at room temperature instead of high temperature [17].

1.3.2 Bottom-up methods

For the bottom-up approach, solution-phase chemical methods by oxidative condensation have been successfully applied to produce GQDs. Fig. 11c shows the scheme of the overall HBC was carbonized under high temperature, hydrothermal treatment, microwave. [Chemically doped fluorescent ...] The starting material is usually organic small molecules or other small species that have doping elements themselves. The hydrothermal (or solvothermal) method is a feasible way to make GQDs, which can be considered as an “environmentally friendly transformation tool” that can convert raw materials with complicated ingredients into the products. As one typical example, milk, known to have N-containing species, was “converted” into N-CQDs with the size of around 3 nm by the hydrothermal method. Also, grass, as a starting material, was selected to synthesize 3–5 nm N-CQDs via the hydrothermal method. The most outstanding advantage of using the hydrothermal method for N-CQDs is reflected in the widely used precursors that are not only restricted to materials existing in nature, but extended to many organic small molecules containing carbon and dopants. For example, N-doped GQDs (N-GQDs) were easily prepared by the hydrothermal method using citric acid (CA) as carbon source, and urea or ethylene diamine as N source [18-20].

1.4 Modification (functionalization) of graphene quantum dots

If GQD synthesis is considered in its infancy it could be said that the functionalization and assembly of GQDs are at their conception. Functionalization of GQDs has the potential to alter photoluminescence, biocompatibility, and electronic properties and to reduce non-radiative recombination to enhance optical properties and quantum yields. Functionalization has also been shown to produce GQDs with good quantum yields. Similar to the methods used to produce GQDs, modification of GQDs can be achieved by two different approaches; prefabrication modification of parent materials and modification post GQD synthesis.

1.4.1 Pre-Fabrication Modification

Nitrogen doping of graphene sources is common due to its comparable atomic size to carbon and five valence electrons. A hydrothermal approach for the production of nitrogen-doped GQDs was reported. The top-down approach was used to hydrothermally cut nitrogen-doped graphene into nitrogen-doped GQDs. The glutathione-functionalized GQDs (GQDs@GSH) was produced via a one-step pyrolysis method. Citric acid and glutathione were mixed, heated, dissolved into Milli-Q ultrapure water and separated via column chromatography, producing GQDs@GSH with sizes ranging from 6 to 60 nm. The glutathione functionalization was also shown to improve both biological compatibility and fluorescence quantum yield (up to 33.6%) [21-22].

1.4.2 Post-Fabrication Modification

As reported previously, surface functionality have many effects on the photoluminescent properties of GQDs. Carboxylic acid and epoxy groups induce non-radiative recombination of electron-hole pairs, inhibiting the intrinsic state emission. Modifications included reduction with NaBH_4 to convert carbonyl, epoxy, and amido moieties to hydroxyl groups and reaction with alkylamines to convert $-\text{COOH}$ and epoxy groups to $-\text{CONHR}$ and $-\text{CNHR}$ groups. Both types of modification lead to a PL blue-shift since reducing the non-radiative recombination processes. A modified electrochemical approach was used to synthesize catalytically active nitrogen-doped GQDs, where tetrabutylammonium perchlorate in acetonitrile was used as an electrolyte to insert nitrogen atoms into the GQDs in situ. The N-GQDs were produced by continuously scanning over a potential window of ± 3.0 V. This applied potential was high enough to drive the electrolyte ions into the graphene layers and oxidize the C-C bonds of the graphene sheets. The resulting PL spectra were blue shifted in contrast to the nitrogen-free GQDs. The change in emission was due to the strong electron-withdrawing properties of nitrogen atoms within the conjugated carbon plane [23].

1.5 Motivation

Fluorescent materials produce visible or invisible light as a result of incident light of a different wavelength. The effect ceases as soon as the source of excitement is removed. Fluorescent organic dyes and semiconductor quantum dots have a bunch of invaluable benefits and are excellent materials for biosensing, labeling and bioimaging. However, they

may be risky to both human body and the environment as well, which is a growing concern and inspiring more and more effects in scientists over the world. Graphene quantum dots have been considered as a new class of environment friendly and non-toxicity alternatives to traditional fluorescence materials. The biocompatibility and biosafety are far more than satisfactory.

In recent years, as consequence of health concerns and biological hazards, GQDs have become the center of significant research efforts to develop low-toxicity, eco-friendly alternatives that have the desirable performance characteristics of QDs. Furthermore, GQDs are superior in terms of their excellent characteristics such as high photostability against photobleaching and blinking, biocompatibility, excellent solubility in different solvents, and tunable band gap. For these reasons, GQDs have withdrawn great attention from both academic and industry.

The bottom-up strategy has attracted a great attention owing to an eco-friendly, facile and effective synthetic route for mass production of high quantum-yield GQDs. To date, extreme efforts have been devoted to find out plenty of bottom-up approaches for preparing the GQDs. Particularly, through choosing different molecules as raw materials, wide range of doped or functionalized GQDs with tunable properties can be obtained for various purposes, but the properties of these chemically modified GQDs are still unclear and are required more efforts to gain insight.

Reference

- [1]. X. L. Li, X. R. Wang, L. Zhang, S. W. Lee, H. G. Dai, Chemically derived, ultrasmooth graphene nanoribbon semiconductors, *Science* 319 (2008) 1229-1232.
- [2]. L. A. Ponomarenko, F. Schedin, M. I. Katsnelson, R. Yang, E.W. Hill, K. S. Novoselov, A. K. Geim, Chaotic dirac billiard in graphene quantum dots, *Science* 320 (2008) 356-358.
- [3]. X. Xu, R. Ray, Y. Gu, H. J. Ploehn, L. Gearheart, K. Raker, W. A. Scrivens, Electrophoretic analysis and purification of fluorescent single-walled carbon nanotube fragments, *J. Am. Chem. Soc.* 126 (2004) 12736-12737.
- [4]. S.Y. Ju, W. P. Kopcha, F. Papadimitrakopoulos, *Science* 323 (2009) 1319-1323.
- [5]. S. J. Yu, M. W. Kang, H. C. Chang, K. M. Chen, Y. C. Yu, Bright fluorescent nanodiamonds: No photobleaching and low cytotoxicity, *J. Am. Chem. Soc.* 127 (2005) 17604-17605.
- [6]. S. N. Baker, G. A. Baker, Luminescent carbon nanodots: Emergent nanolights, *Angew. Chemie. Chem. Int. Ed.* 49 (2010) 6726-6744.
- [7]. Y. Li, Y. Hu, Y. Zhao, G. Shi, Q. L. Deng, Y. B. Hou, L. T. Qu, An electrochemical avenue to green-luminescent graphene quantum dots as potential electron-acceptors for photovoltaics, *Adv. Mater.* 23 (2011) 776-780.
- [8]. X. Sun, Z. Liu, K. Welsher, J. T. Robinson, A. Goodwin, S. Zaric, H. Dai, Nanographene oxide for cellular imaging and drug delivery, *Nano Res.* 1 (2008) 203-212.

- [9]. J. Shen, Y. Zhu, X. L. Yang, C. Z. Li, Graphene quantum dots: Emergent nanolights for bioimaging, sensors, catalysis and photovoltaic devices, *Chem. Commun.* 48 (2012) 3686-3899.
- [10] J. H. Shen, Y. H. Zhu, X. Yang, J. Zong, J. M. Zhang, C. Z. Li, One-pot hydrothermal synthesis of graphene quantum dots surface-passivated by polyethylene glycol and their photoelectric conversion under near-infrared light, *New J. Chem.* 36 (2012) 97-101.
- [11]. D. Y. Pan, J. C. Zhang, Z. Li, M. H. Wu, Hydrothermal route for cutting graphene sheets into blue-luminescent graphene quantum dots, *Adv. Mater.* 22 (2010) 734-738.
- [12]. J. H. Shen, Y. H. Zhu, C. Chen, X. L. Yang, C. Z. Li, Facile preparation and upconversion luminescence of graphene quantum dots, *Chem. Commun.* 47 (2011) 2580-2582.
- [13]. X. Yan, X. Cui, Large, solution-processable graphene quantum dots as light absorbers for photovoltaics, *Nano Lett.* 10 (2010) 1869-1973.
- [14]. R. Liu, D. Wu, X. Feng, K. Mullen, Bottom-up fabrication of photoluminescent graphene quantum dots with uniform morphology, *J. Am. Chem. Soc.* 133 (2011) 15221-15223.
- [15]. H. Liu, Y. Liu, D. Zhu, Chemical doping of graphene, *J. Mater. Chem.* 21 (2011) 3335-3345.
- [16]. Y. Li, Z. Zhou, P. Shen, Z. F. Chen, Spin gapless semiconductor-metal-half-metal properties in nitrogen-doped zigzag graphene nanoribbons, *ACS Nano* 3 (2009) 1952-1958.

- [17]. Y. Li, Y. Zhao, H. Cheng, Y. Hu, G. Q. Shi, L. Dai, L. Qu, Nitrogen-doped graphene quantum dots with oxygen-rich functional groups, *J. Am. Chem. Soc.* 134 (2012) 15-18.
- [18]. C. Hu, Y. Liu, Y. L. Yang, J. Cui, Z. Huang, Y. Wang, L. Yang, H. Wang, Y. Xiao, J. Rong, One-step preparation of nitrogen-doped graphene quantum dots from oxidized debris of graphene oxide, *J. Mater. Chem. B* 1 (2013) 39-42.
- [19]. J. Peng, W. Gao, B. K. Gupta, Z. Liu, R. Romero-Aburto, L. Ge, L. Song, L. B. Alemany, X. Zhan, G. Gao, S. A. Vithayathil, B. A. Kaiparettu, A. A. Marti, T. Hayashi, J. J. Zhu, P. M. Ajayan, Graphene quantum dots derived from carbon fibers, *Nano Lett.* 12 (2012) 844-849.
- [20]. X. Dong, D. Fu, W. Fang, Y. Shi, P. Chen, L. J. Li, Doping single-layer graphene with aromatic molecules, *Small* 5 (2009) 1422-1426.
- [21]. G. Eda, Y. Y. Lin, C. Mattevi, H. Yamaguchi, H. A. Chen, I. S. Chen, C. W. Chen, M. Chhowalla, Blue photoluminescence from chemically derived graphene oxide, *Adv. Mater.* 22 (2010) 505-509.
- [22]. H. Tetsuka, H. Tetsuka, R. Asahi, A. Nagoya, K. Okamoto, I. Tajima, R. Ohta, A. Okamoto, Optically tunable amino-functionalized graphene quantum dots, *Adv. Mater.* 24 (2012) 5333-5338.
- [23]. H. Liu, C. Quin, Y. G. Wei, X. Lin, G. G. Gao, F. Y. Li, X. S. Qu, Copper-complex-linked polytungsto-bismuthate(-antimonite) chain containing sandwich Cu (II) ions partially modified with imidazole ligand, *Inorg. Chem.* 47 (2008) 9413-9419.
- [24]. S. K. Sahoo, D. Sharma, R. K. Bera, G. Crisponi, J. F. Callan, Iron (III) selective molecular and supramolecular fluorescent probes, *Chem. Soc. Rev.* 41 (2012) 7195-7227.

CHAPTER 2: One-pot synthesis of N-doped graphene quantum dots as a fluorescent sensing platform for Fe³⁺ ions detection

2.1 Introduction

The development of new types of quantum dots (QDs) has received increasing attention recently, as QDs can enable the fabrication of new structures or devices with extraordinary functions and properties to replace commonly used semiconductor nanocrystals, which are expensive and contain cytotoxic heavy metal constituents. Among QDs, zero-dimensional graphene quantum dots (GQDs) have been studied on both experimental and theoretical fronts and show marvelous optical properties that are directly associated with quantum confinement and edge effects [1-2]. Like carbon based luminescence nanomaterials [3-6], the GQDs present some fascinating characteristics that may not be observed in traditional semiconductor quantum dots, such as low toxicity, excellent solubility, high and stable luminescence, robust chemical inertness, good biocompatibility and a tunable band gap. Therefore, the GQDs have potential for light-emitting, photovoltaic, bioimaging, and a new generation of detection applications [7, 8]. Consequently, the development of various chemical methods for controllable synthesis of GQDs has received tremendous attention [9]. There are two major strategies for synthesizing GQDs, i.e., top-down and bottom-up methods. The former approaches involve the exfoliation of graphite into graphene sheets, followed the cutting of graphene sheets into GQDs. Therefore, the top-down method may be limited by low product yield and harsh conditions due to the use of a toxic organic solvent and strong acid/oxidant [2, 10-12]. However, the bottom-up approaches refer to the construction of GQD from small organic precursor molecules through catalytic or thermal treatment, resulting in

the environmentally-friendly production of large scale GQDs with uniform size of distribution and morphology [13, 14]. Physical and chemical properties including chemical reactivity, electronic structure, and optical properties of carbon materials (such as carbon nanotubes and graphene) can be effectively tuned by doping with heteroatoms. Nitrogen (N) atoms have been used widely for chemical doping of carbon materials due to a comparable atomic size and five valence electrons for bonding with carbon atoms. N-doped into graphene was highly effective in modulating its band gap to achieve new properties for device applications [15, 16]. Due to the remarkable quantum confinement and edge effects of GQDs, direct substitution with nitrogen in GQDs lattice can drastically modulate the chemical and electronic properties and offer more active sites, thus leading to unexpected phenomena which could be extensively applied in various fields. Recently, N-doped GQDs (N-GQDs) have been synthesized through hydrothermal or electrochemical strategies which are based on cutting graphene oxide (GO) and its reduction. However, synthesis of GO typically takes several days and requires lots of strong chemical acid and oxidant in a series of chemical treatments of the bulk graphite powder [17, 18].

Fluorescent sensors have been considered as useful method to detect metal ions due to their high sensitivity, selectivity and fast detection. However fluorescent semiconductor quantum dots and metal nanoparticles have attracted considerable attention as fluorescent sensing materials for the detection of metal ions, they are limited by their toxicity and expensive synthesis method. Recently, fluorescent GQDs have gained great attention as alternative to semiconductor quantum dots in the detection of metal ions due to their low toxicity, excellent biocompatibility, and good photostability. Despite aforementioned method

to synthesize GQDs, it is still necessary to develop a promising method for GQDs with simple, low-cost, and environmentally friendly approach.

In line with the intensive research on GQDs and N-GQDs, we report here a facile one step synthesis of GQDs and N-GQDs from the hydrothermal carbonization of citric acid (CA) in the presence of ammonia. Without the use of a strong acid, oxidant and other chemical reagent, the GQDs and N-GQDs were synthesized in an aqueous solution, implying the process proposed here is relatively simple and environmentally friendly. The N-GQDs synthesized here have a uniform size distribution of 3-4 nm with a thickness of a few graphene layers, and the nitrogen atoms were successfully doped into the graphene lattice. Furthermore, the prepared GQDs and N-GQDs show different fluorescence of green and blue colors, respectively, due to the electronic structure change by the successful introduction of nitrogen atoms. With these features of the prepared GQDs, we have also demonstrated a novel fluorescent sensing application of N-GQDs for detection of Fe³⁺ ions.

2.2 Experiment

2.2.1 Synthesis of GQDs and N-GQDs

The N-GQDs were synthesized by carbonization of CA (99%, Sigma-Aldrich) with ammonia through hydrothermal treatment. In brief, 40 ml of a CA aqueous solution (1mg/ml) and an ammonia aqueous solution (2, 5, and 8 ml, 25% wt) were transferred into a Teflon-lined autoclave and were heated at 200°C for 3h. After cooling to room temperature, the pH of the light yellow N-GQDs solution was tuned to 8 with adding NaOH solution (1mg/ml) dropwise. The light yellow N-GQDs solution was dialyzed in dialysis tubing (3000 Da, Spectrum Lab. Inc) against DI water for 4 hours to remove impurities and excess ammonia. After dialysis, an aqueous suspension of N-GQDs was obtained. For the synthesis of GQDs, a

similar process was carried out without adding an ammonia solution, and a light yellow solution of GQDs was obtained.

2.2.2 Characterizations

Surface morphologies and topographies of the GQDs and N-GQDs were determined by atomic force microscopy (AFM; Veeco, Dimension 3100), and the microstructures were observed with a transmission electron microscope (TEM; JEOL, JEM-2100F). X-ray photoelectron spectroscopy (XPS; Thermo Fisher) measurements were performed using monochromatic AlK α radiation ($h\nu = 1486.6$ eV). The UV-vis absorption spectra of GQDs and N-GQDs were measured with Specord 210 UV-vis spectrophotometer. Raman Spectroscopy was performed from 1000 to 2000 cm⁻¹ at room temperature using DXR Raman spectrometer (Thermo Scientific) with an incident laser at a wavelength of 532 nm. The Fourier transform infrared (FT-IR) spectra were measured to verify the functional groups with a Nicolet IR 200 FT-IR spectrometer (Thermo Scientific). Photoluminescence spectra were taken at room temperature using a HORIBA FluoroMax-4P spectrophotometer. Because of low quantum yield of GQDs, concentration of GQDs (0.6 mg/ml) was higher than N-GQDs (0.1 mg/ml) for clear photoluminescence spectra. For the detection of various metal ions, FeCl₃, AgNO₃, CuCl₂, NaCl, KCl, LiNO₃, MnCl₂, Cr(NO₃)₃, CaCl₂, and Zn(NO₃)₂ were used as various metal ion sources. 0.5 ml of metal ion solution with various concentrations was added into 1.0 mL of N-GQDs solution (0.03 mg/ml), and after reaction for 50 s, the PL spectra were recorded with excitation with a 325 nm.

2.3 Results and discussion

Fig. 3 presents the process used to synthesize N-GQDs, where the CA is carbonized and converted into N-GQDs in the presence of ammonia through the hydrothermal process at 200°C for 3 hr, followed by a further purification process to obtain an aqueous solution of N-GQDs. Typically, when 40 ml of a CA aqueous solution (1 mg/ml) and 8 ml of an ammonia aqueous solution were used here, we obtained the N-GQDs aqueous solution with concentration of 4.91 mg/ml. N atoms from ammonia were introduced into the graphene lattice through the high temperature hydrothermal process. When CA was solely used without the addition of ammonia, the undoped GQDs were obtained from the hydrothermal process.

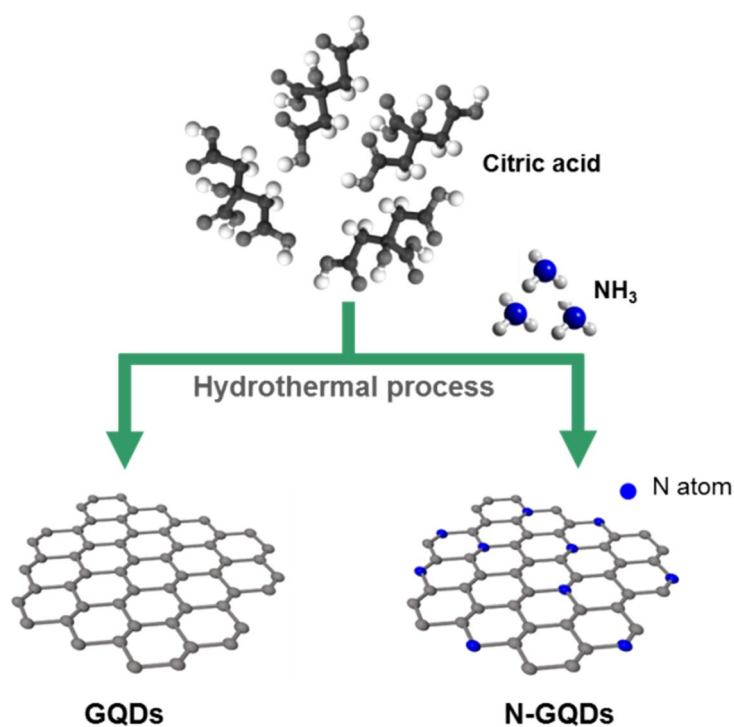


Figure 3 Synthesis illustration of GQDs and N-GQDs by the carbonization of citric acid with ammonia through the hydrothermal process.

Fig. 4a shows a transmission electron microscopy (TEM) image of the N-GQDs prepared in this work. It can be seen that the obtained N-GQDs are relatively uniform in size without agglomeration and are in the range of 2-8 nm. The size distribution of N-GQDs in Fig. 4b shows that the average diameter of N-GQDs is about 3.5 nm. The high resolution TEM (HRTEM) image (inset of Fig. 4a) reveals the high crystallinity of the N-GQDs. These exhibited a lattice parameter of 0.25 nm, which is similar to (1120) lattice fringes of graphene [19]. These results indicate the transformation of CA with ammonia resulted in high quality N-GQDs through the hydrothermal process, and their crystal structures were comparable to that of GQD from graphite. AFM image of N-GQDs in Fig. 4c shows the topographic morphology of N-GQDs, and the heights of N-GQDs are primarily between 0.5-1 nm. The average height of N-GQDs is about 1.2 nm, and more than 70% of the N-GQDs are less than 2 nm in height, suggesting that most N-GQDs consist of 1-3 graphene layers. In addition, TEM and AFM measurements of the undoped GQDs were taken. The average size and height of the undoped GQDs are 4.6 and 1.8 nm, respectively. These results indicate that the microstructure of the N-GQDs, such as their size and height, did not significantly change due to the functionalization of N atoms.

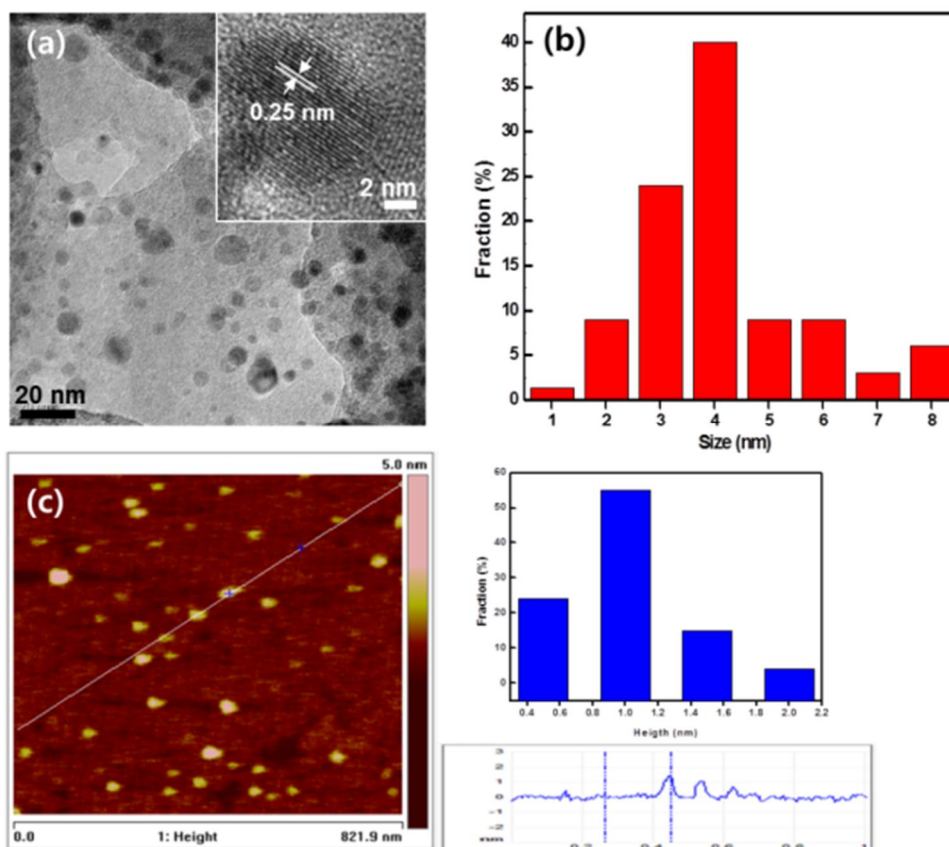


Figure 4 (a) TEM image and (b) the lateral size distributions of N-GQDs. (c) AFM image of the N-GQDs and the height distributions. Inset of (a) shows HRTEM image of N-GQDs.

Effectiveness of the N atoms doping of GQDs was evaluated with FT-IR spectra, XPS, and Raman spectroscopy. Fig. 5a shows the FT-IR spectrums of GQDs and N-GQDs with various ammonia contents. The FT-IR spectrum of GQDs exhibits absorption peaks of the deformation of C-O and the stretching vibration of C=O in the carboxyl group at 1384 and 1605 cm^{-1} , respectively. In addition, the broad absorption band around 3401 cm^{-1} can be assigned to the stretching vibration of the H-bonded associated -OH group. The FTIR spectra of N-GQDs present new peaks with the absorption peaks of oxygen-related groups in the

GQDs. In the FT-IR spectra of N-GQDs, two new peaks at 1019 and 3146 cm^{-1} are corresponded to the C-N in-plane bending vibration and N-H bending vibration, which indicate successful nitrogen functionalization in the lattice of N-GQDs. Furthermore, XPS measurements of GQDs and N-GQDs with various ammonia contents were carried out to determine the composition of the N-GQDs. The XPS wide scan of GQDs displays only the presence of oxygen (O 1s \sim 532 eV) and carbon (C 1s \sim 285 eV) peaks, while that of N-GQDs shows a pronounced nitrogen peak (N 1s \sim 400 eV) with oxygen and carbon peaks as seen in Fig. 5b. To further evaluate the N configuration in N-GQDs, N 1s core level XPS spectra of N-GQDs from the use of 0.8 ml ammonia (0.8N-GQDs) was investigated as shown in Fig. 5c. The N 1s spectrum can be deconvoluted into two group peaks where pyrrolic N and graphitic or quaternary N atoms are centered at the binding energy of 400.1 and 401.6 eV, respectively. Additionally, the C 1s core level XPS spectra of 0.8N-GQDs presents the C-C bond at 284.4 eV, C-N bond at 285.7 eV, the carbon hydroxyl groups (C-OH) at 286.6 eV and carboxylate carbon group (O-C=O) at 288.7 eV (Fig. 5d). With the amount of ammonia used at 0.2, 0.5, and 0.8 ml, N/C atomic ratios were also calculated to be 8.3, 10.0, and 11.1%, respectively. These results confirm the successful introduction of N in N-GQDs and are also consistent with the corresponding FTIR spectroscopy results. UV-Vis absorption spectra of GQDs shows a typical absorption peak at about 330 nm, which is assigned to the $\pi \rightarrow \pi^*$ transition of the aromatic sp^2 domain (see Fig. ESI-3). On the other hand, the UV-visible absorption spectra of the N-GQDs show an absorption peak at 315 nm, which is a clear blue shift by 15 nm with respect to that of GQDs. This result reveals that doping by N atoms affected the absorption properties of N-GQDs.

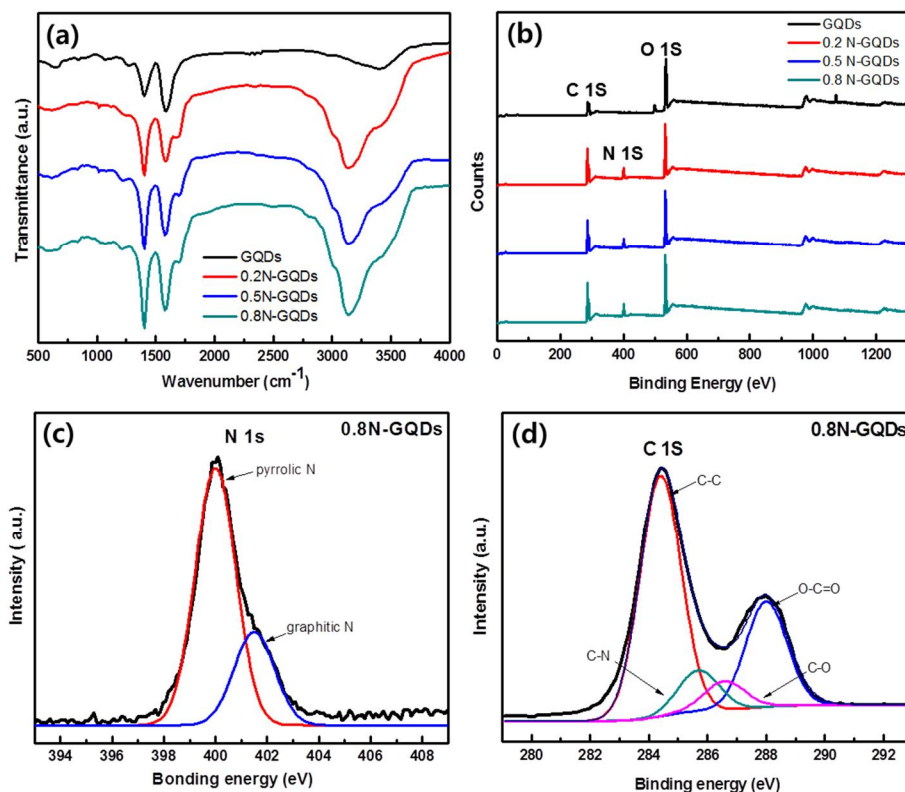


Figure 5 (a) FT-IR Spectra and (b) survey XPS spectra of GQDs and N-GQDs with various contents of ammonia. (c) N 1s and (d) C 1s core-level XPS spectra of 0.8N-GQDs.

To further explore the optical properties of N-GQDs, PL characterization was carried out. Fig. 6a presents the PL emission spectra of the aqueous solutions of GQDs and N-GQDs under excitation with a 325 nm wavelength. Compared to GQDs, N-GQDs show considerably stronger PL emission, and the intensity of N-GQDs was about 1.5 times higher than that of GQDs. The peak position of N-GQDs is at about 420 nm, which is blue-shifted from that of GQDs (530 nm). Inset images of Fig. 6a include photographs of the aqueous solutions of GQDs and N-GQDs taken under irradiation by a 365 nm lamp (20 W). It is clearly observed that the GQDs exhibit a green fluorescence color, while the N-GQDs exhibit

a blue fluorescence color with higher brightness. Using quinine sulfate as the standard, the PL quantum yield of the N-GQDs was measured to be about 30.7%, which was higher than that of GQDs (4.5%). Since the GQDs and N-GQDs have similar size and thickness, the blue shift and the intensity increase in the PL of N-GQDs should originate from the change in the electronic structure of N-GQDs due to the N doping of GQDs. It has been reported that the incorporation of hetero atoms in the graphene lattice would disrupt sp^2 hybridization of carbon atoms [22]. In addition, insolated sp^2 hybridized clusters within a carbon-oxygen matrix could lead to band gaps consistent with blue emission due to the localization of electron-hole pairs [23]. So, the strong electron affinity of N atoms, doping in pyridinic sites of N-GQDs, could induce a blue shift in the PL measurement. Indeed, this phenomenon has been reported in experimental observations and quantum-mechanical calculations [24, 25]. The initial concentration of ammonia in the hydrothermal treatment can also affect the photoluminescence. By changing the amount of ammonia from 0.2 to 0.8 ml, the PL peak positions of N-GQDs shift from 435 to 410 nm, as shown in Fig. 6b, indicating the tunable photoluminescence by the control of N-atom ratio. For a detailed PL study of N-GQDs, we carried out PL measurements by using different excitation wavelengths, as shown in Fig. 6c. As the excitation wavelength is changed from 300 to 500 nm, the PL peaks of N-GQD shift to longer wavelengths and its intensity decreased gradually. On excitation at 320 nm the PL spectrum exhibits the strongest peak at about 420 nm with Stokes shift of 100 nm, which is consistent with a previously report [11]. Similarly, the GQDs show excitation-dependent PL behavior with the strongest peak at 500 nm in response to excitation at a wavelength of 400 nm.

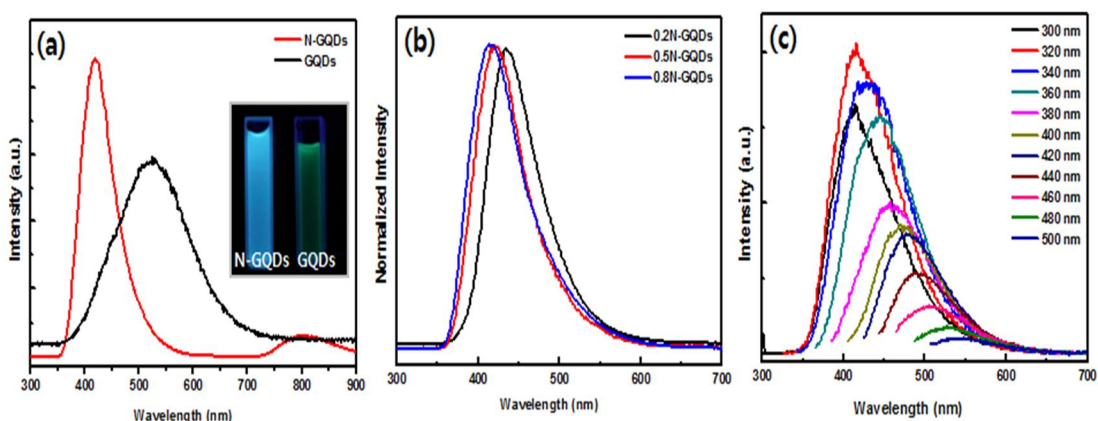


Figure 6 (a) PL spectra of GQDs and N-GQDs. The inset of (a) is a photograph image of N-GQDs (left) and GQDs (right) in water under 365 nm UV lamp irradiation. (b) PL spectra of N-GQDs with various contents of ammonia. (c) The excitation-dependent PL spectra of N-GQDs.

To explore the fluorescence sensing application of N-GQDs, we performed PL measurements in the presence of various metal ions (100 μM) such as Li^+ , Na^+ , Fe^{3+} , K^+ , Ca^{2+} , Zn^{2+} , Mn^{2+} , Ag^+ , Cu^{2+} , Cr^{3+} , Cd^{3+} , Hg^{2+} , and Pb^{2+} . As shown in Fig. 7a, it is noteworthy that the PL intensity of N-GQDs resulted in the strongest quenching effect in the presence of Fe^{3+} ions, whereas no notable PL quenching effect was found in the presence of different metal ions. The inset images of Fig. 7a present the fluorescence of N-GQDs solutions with no metal ions, Fe^{3+} , and Cu^{2+} ions under a UV lamp. The N-GQDs solution emitted strong blue color with no metal ion added. In the addition of Fe^{3+} ions, the fluorescence was quenched completely, while no notable fluorescence quenching was observed in the presence of Cu^{2+} ions. In addition to this high selectivity of N-GQDs on Fe^{3+} ions, their sensitivity was investigated. As shown in Fig. 7b, the concentration dependent fluorescence measurements of N-GQDs with various concentrations of Fe^{3+} ions were monitored to prove the feasibility of

Fe³⁺ ions detection. A notable decrease in PL intensity of N-GQDs was observed as the concentration of Fe³⁺ ions was increased from 1 μM to 500 μM. The inset of Fig. 7b shows a correlation between the fluorescence enhancement factors ((F-F₀)/F₀), defined as change in emission by change in concentration, and the concentration of Fe³⁺ ions, which exhibits the linear relation in the low concentration and the saturated curve in the high concentration of Fe³⁺ ions. It is believed that Fe³⁺ metal ions could form metal hydroxides by coordinating with hydroxyl groups on the edge and surface of N-GQDs. The as-formed metal complexes would facilitate charge transfer and restrain the recombination of excitons, resulting in the PL quenching behavior [24]. Therefore, the N-GQDs synthesized here could be the appropriate sensing materials with high selectivity and sensitivity for the detection of Fe³⁺ ions.

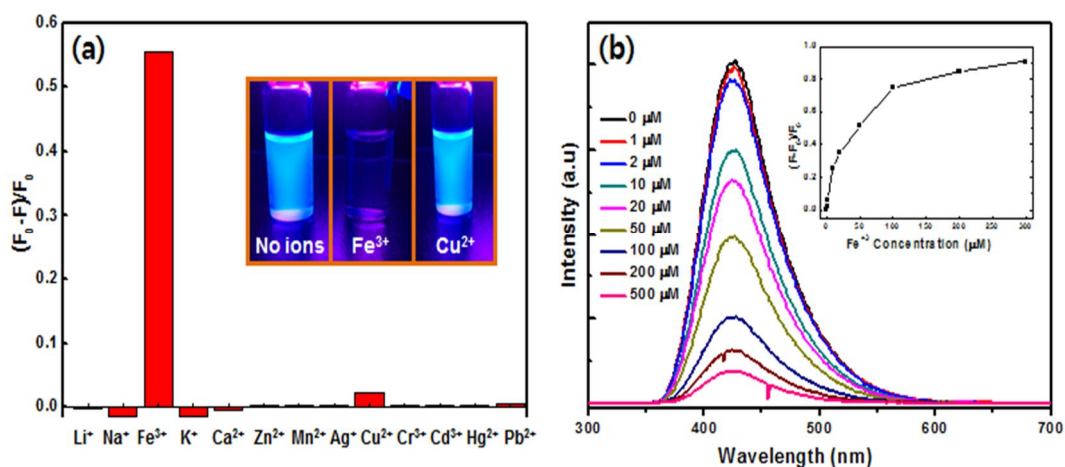


Figure 7 (a) The fluorescence enhancement factors [(F-F₀)/F₀] of the N-GQDs solutions in the presence of various metal ions at the concentration of 100 μM. Insets are the photograph images of N-GQDs solutions with no metal ion (left), presence of Fe³⁺

(middle) and Cu^{2+} (right) ions under 365 nm UV light. (b) PL spectra of N-GQDs with various concentrations of Fe^{3+} ions.

2.4 Conclusion

We have demonstrated a facile synthesis of N-GQDs from the carbonization of citric acid through hydrothermal treatment in the presence of ammonia. These synthesized N-GQDs were mostly composed of 1-3 layers with a uniform size of about 3.5 nm, and their N/C ratios were controlled by the amount of ammonia. The N-GQDs also exhibit bright blue-luminescence with higher PL quantum yield than GQDs which show green-luminescence. Furthermore, we have demonstrated that N-GQDs can be used as fluorescence probes for the detection of Fe^{3+} ions with high selectivity and sensitivity. Our approach represents a green, inexpensive and convenient method for large-scale production of N-GQDs. The N-GQDs synthesized by this process can potentially be used in various novel optoelectronics and bioimaging applications due to their tunable optical properties, low cytotoxicity, excellent solubility and low cost.

Reference

- [1]. X. L. Li, X. R. Wang, L. Zhang, S. W. Lee, H. G. Dai, Chemically derived, ultrasmooth graphene nanoribbon semiconductors, *Science* 319 (2008) 1229-1232.
- [2]. L. A. Ponomarenko, F. Schedin, M. I. Katsnelson, R. Yang, E.W. Hill, K. S. Novoselov, A. K. Geim, Chaotic dirac billiard in graphene quantum dots, *Science* 320 (2008) 356-358.

- [3]. X. Xu, R. Ray, Y. Gu, H. J. Ploehn, L. Gearheart, K. Raker, W. A. Scrivens, Electrophoretic analysis and purification of fluorescent single-walled carbon nanotube fragments, *J. Am. Chem. Soc.* 126 (2004) 12736-12737.
- [4]. S.Y. Ju, W. P. Kopcha, F. Papadimitrakopoulos, *Science* 323 (2009) 1319-1323.
- [5]. S. J. Yu, M. W. Kang, H. C. Chang, K. M. Chen, Y. C. Yu, Bright fluorescent nanodiamonds: No photobleaching and low cytotoxicity, *J. Am. Chem. Soc.* 127 (2005) 17604-17605.
- [6]. S. N. Baker, G. A. Baker, Luminescent carbon nanodots: Emergent nanolights, *Angew. Chemie. Chem. Int. Ed.* 49 (2010) 6726-6744.
- [7]. Y. Li, Y. Hu, Y. Zhao, G. Shi, Q. L. Deng, Y. B. Hou, L. T. Qu, An electrochemical avenue to green-luminescent graphene quantum dots as potential electron-acceptors for photovoltaics, *Adv. Mater.* 23 (2011) 776-780.
- [8]. X. Sun, Z. Liu, K. Welsher, J. T. Robinson, A. Goodwin, S. Zaric, H. Dai, Nanographene oxide for cellular imaging and drug delivery, *Nano Res.* 1 (2008) 203-212.
- [9]. J. Shen, Y. Zhu, X. L. Yang, C. Z. Li, Graphene quantum dots: Emergent nanolights for bioimaging, sensors, catalysis and photovoltaic devices, *Chem. Commun.* 48 (2012) 3686-3899.
- [10] J. H. Shen, Y. H. Zhu, X. Yang, J. Zong, J. M. Zhang, C. Z. Li, One-pot hydrothermal synthesis of graphene quantum dots surface-passivated by polyethylene glycol and their photoelectric conversion under near-infrared light, *New J. Chem.* 36 (2012) 97-101.

- [11]. D. Y. Pan, J. C. Zhang, Z. Li, M. H. Wu, Hydrothermal route for cutting graphene sheets into blue-luminescent graphene quantum dots, *Adv. Mater.* 22 (2010) 734–738.
- [12]. J. H. Shen, Y. H. Zhu, C. Chen, X. L. Yang, C. Z. Li, Facile preparation and upconversion luminescence of graphene quantum dots, *Chem. Commun.* 47 (2011) 2580–2582.
- [13]. X. Yan, X. Cui, Large, solution-processable graphene quantum dots as light absorbers for photovoltaics, *Nano Lett.* 10 (2010) 1869–1973.
- [14]. R. Liu, D. Wu, X. Feng, K. Mullen, Bottom–up fabrication of photoluminescent graphene quantum dots with uniform morphology, *J. Am. Chem. Soc.* 133 (2011) 15221–15223.
- [15]. H. Liu, Y. Liu, D. Zhu, Chemical doping of graphene, *J. Mater. Chem.* 21 (2011) 3335–3345.
- [16]. Y. Li, Z. Zhou, P. Shen, Z. F. Chen, Spin gapless semiconductor-metal-half-metal properties in nitrogen-doped zigzag graphene nanoribbons, *ACS Nano* 3 (2009) 1952–1958.
- [17]. Y. Li, Y. Zhao, H. Cheng, Y. Hu, G. Q. Shi, L. Dai, L. Qu, Nitrogen-doped graphene quantum dots with oxygen-rich functional groups, *J. Am. Chem. Soc.* 134 (2012) 15–18.
- [18]. C. Hu, Y. Liu, Y. L. Yang, J. Cui, Z. Huang, Y. Wang, L. Yang, H. Wang, Y. Xiao, J. Rong, One-step preparation of nitrogen-doped graphene quantum dots from oxidized debris of graphene oxide, *J. Mater. Chem. B* 1 (2013) 39–42.

- [19]. J. Peng, W. Gao, B. K. Gupta, Z. Liu, R. Romero-Aburto, L. Ge, L. Song, L. B. Alemany, X. Zhan, G. Gao, S. A. Vithayathil, B. A. Kaiparettu, A. A. Marti, T. Hayashi, J. J. Zhu, P. M. Ajayan, Graphene quantum dots derived from carbon fibers, *Nano Lett.* 12 (2012) 844-849.
- [20]. X. Dong, D. Fu, W. Fang, Y. Shi, P. Chen, L. J. Li, Doping single-layer graphene with aromatic molecules, *Small* 5 (2009) 1422-1426.
- [21]. G. Eda, Y. Y. Lin, C. Mattevi, H. Yamaguchi, H. A. Chen, I. S. Chen, C. W. Chen, M. Chhowalla, Blue photoluminescence from chemically derived graphene oxide, *Adv. Mater.* 22 (2010) 505-509.
- [22]. H. Tetsuka, H. Tetsuka, R. Asahi, A. Nagoya, K. Okamoto, I. Tajima, R. Ohta, A. Okamoto, Optically tunable amino-functionalized graphene quantum dots, *Adv. Mater.* 24 (2012) 5333-5338.
- [23]. H. Liu, C. Quin, Y. G. Wei, X. Lin, G. G. Gao, F. Y. Li, X. S. Qu, Copper-complex-linked polytungsto-bismuthate(-antimonite) chain containing sandwich Cu (II) ions partially modified with imidazole ligand, *Inorg. Chem.* 47 (2008) 9413-9419.
- [24]. S. K. Sahoo, D. Sharma, R. K. Bera, G. Crisponi, J. F. Callan, Iron (III) selective molecular and supramolecular fluorescent probes, *Chem. Soc. Rev.* 41 (2012) 7195-7227.

CHAPTER 3: Ultraviolet light sensor based on graphene quantum dots/reduced graphene oxide hybrid film

3.1 Introduction

Due to its superior physical properties, such as high room-temperature mobility ($250,000\text{m}^2/\text{V}\cdot\text{s}$) and outstanding thermal conductivity (5000 W/mK), graphene has attracted considerable attention in both academic and industry area for potential applications including semiconducting devices, optoelectronic devices, and energy storage devices [1-3]. However, graphene shows the poor photoresponsivity ($\sim 10^{-2}\text{ A/W}$) due to the weak light absorption in graphene, which impedes its application in optoelectronic devices [4]. Fortunately, graphene quantum dots (GQDs) are a type of zero dimensional graphene with lateral dimensions of less than 100 nm , and they have received enormous attention due to their unique chemical, electronic, and optical properties from quantum confinement and edge effects [5,6]. They also have stable photoluminescence, low cytotoxicity, high water solubility and excellent biocompatibility [7]. GQDs are considered as a promising green nanomaterial and an alternative to traditional fluorescent nanocrystals for applications in photocatalysts, sensors, and bioimaging [8]. Therefore, integrating the excellent optical and electrical properties of GQDs and superior physical properties of graphene by the formation of hybrid structures should help generate unique physical properties and offer a potential pathway for constructing all graphene-based material devices with high performance.

Here, we developed a novel ultraviolet (UV) sensor based on GQDs/reduced graphene oxide (RGO) hybrids, showing the high performances of photoresponsivity and detectivity. The GQDs prepared by the carbonization of citric acid (CA) show high quantum

yield and can produce the photogenerated carriers due to the strong absorption of UV light. The RGO film obtained by the thermal reduction of graphene oxide (GO) is employed as a charge transporting layer due to its superior electrical properties [9]. The UV sensor based on GQDs/RGO hybrids was fabricated with a simple and low-cost process and the devices exhibited the enhanced performances, such as photoresponsivity of 8.7×10^2 A/W and specific detectivity of 7.7×10^{13} Jones at a low operating voltage. The high performance of the device is attributed to the efficient transfer of the photogenerated electrons from GQDs to RGO, which was also confirmed by the photoluminescence (PL) quenching of the GQDs/RGO hybrids.

3.2 Experiment

3.2.1 Preparation of Graphene oxide

Graphene oxide (GO) was synthesized using an expanded graphite (grade 1721, Asbury Carbon) by a modified Hummer method described elsewhere [10]. First, the expandable graphite (5 g) was heated for 1 min in a microwave, followed by mixing with concentrated H_2SO_4 (500 mL) under stirring. After the mixture solution was cooled to 0°C in an ice bath, KMnO_4 (30 g) was slowly added with a reaction temperature below 20°C . The mixture was then stirred for 2 h at 35°C to oxidize and exfoliate the graphite. Deionized water (2 L) was slowly added and the diluted mixture was stirred for 1 hour. During the addition of H_2O_2 (500 ml, 30% wt), the colour of the mixture solution changed to dark yellow. The mixture solution was centrifuged and rinsed thoroughly with 10% HCl solution to remove metal ions, followed by washing with deionized water until the GO solution reached a pH of 6. The GO solution was obtained with the concentration of 1.5 mg/mL and was used for further experiments.

3.2.2 Synthesis of GQDs

GQDs were synthesized by the carbonization of CA through the hydrothermal method described in our previous report [11]. CA (500 mg, 30 wt%) was dissolved in 40 ml deionized water and mixed with ammonia solution (0.6 ml, 30 wt%), followed by a hydrothermal procedure at 200°C for 8h. The as-synthesized GQDs solution was dialyzed using a dialysis tube (3000 Da, Spectrum Lab. Inc.) against deionized water for 2 days to remove unreacted ammonia and impurities. The GQDs solution was finally obtained with the concentration of 0.3 mg/ml.

3.2.3 Fabrication of GQDs/RGO UV sensor

The overall fabrication process is shown in Figure 8. The GQDs/RGO hybrid UV sensor was prepared on a SiO₂/Si substrate, where the thickness of SiO₂ is 300 nm. The SiO₂/Si substrate was first treated with UV-ozone (PDS-UV4, Novascan) for 5 min, and the GO solution was then spin-coated at 3000 rpm on the SiO₂/Si substrate. The thermal reduction was performed by heating at 900°C for 30 minutes under an N₂ atmosphere to obtain RGO film. The GQDs solution was sprayed on the prepared RGO film, and then heated at 100°C for 3 min to obtain a strong contact between the GQDs and RGO and for the removal of solvent. Au electrodes (50nm thick) were deposited on the prepared GQDs/RGO hybrid film for the UV sensor devices. The active area of devices is about 4×1 mm².

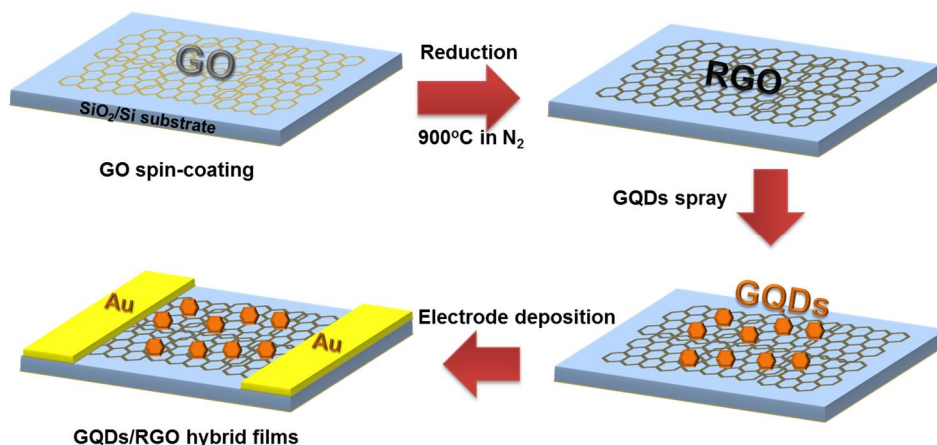


Figure 8 Schematic illustration for the fabrication of GQDs/RGO hybrids UV sensor.

3.2.4 Characterizations

The UV-vis absorption spectra GQDs were measured using a Specord 210 UV-vis spectrophotometer. Atomic force microscopy (AFM) images were recorded using a Veeco, Dimension 3100 with a Si tip operating in the tapping mode, and transmission electron microscopy (TEM) images were acquired using a JEM-2100F (JEOL). X-ray photoelectron spectroscopy (XPS; Thermo Fisher) was performed using monochromatic AlK α radiation ($h\nu=1486.6$ eV). Photoluminescence (PL) spectra were taken at room temperature with a SpectraPro-300i Monochromator (Acton) using a HeCd laser beam with a wavelength of 325 nm and an output of 15 mW power. To estimate HOMO and LUMO energy level of GQDs, linear potential scans (5mV/s) was carried out using a standard three-electrode system, which includes a glassy carbon disk coated with GQDs as the working electrode, a platinum wire as the counter electrode, and a silver wire reference electrode. Electrochemical analysis was recorded in acetonitrile containing 0.1 M tetrabutylammoniumhexafluorophosphate (TBAPF₆, Aldrich) as the supporting electrolyte. The HOMO and LOMO levels in eV as well as band gap (E_g in eV) of GQDs were calculated according to the following equations:

$$E_{\text{HOMO}} = -e(E_{\text{ox}} + 4.4) \quad (1)$$

$$E_{\text{LUMO}} = -e(E_{\text{red}} + 4.4) \quad (2)$$

$$E_{\text{g}} = e(E_{\text{ox}} - E_{\text{red}}) \quad (3)$$

Where E_{ox} and E_{red} are the onset of oxidation and reduction potential, respectively. Electrical measurements and photoresponse were recorded using a Keithley 2400 source meter under ambient condition. The I-V characteristics of the devices were measured in the dark and under UV illumination using a mercury arc lamp (Polam LRF 125W Mercury).

3.3 Results and Discussion

The TEM image of the GQDs in Figure 9a and 9b show that the synthesized GQDs are uniform in size, ranging from 2 and 8 nm in diameter, and are well dispersed without agglomeration. The high resolution TEM (HR-TEM) image in Figure 9b shows that the lattice fringe of GQDs resulted from the high crystallinity of GQDs. The topographic heights of GQDs range from 0.6 to 2 nm with the average height of 1.2 nm, which suggest that most of the GQDs primarily consist of 1-3 graphene layers [12,13]. These results suggest that CA has been successfully transformed into high quality GQDs after hydrothermal treatment.

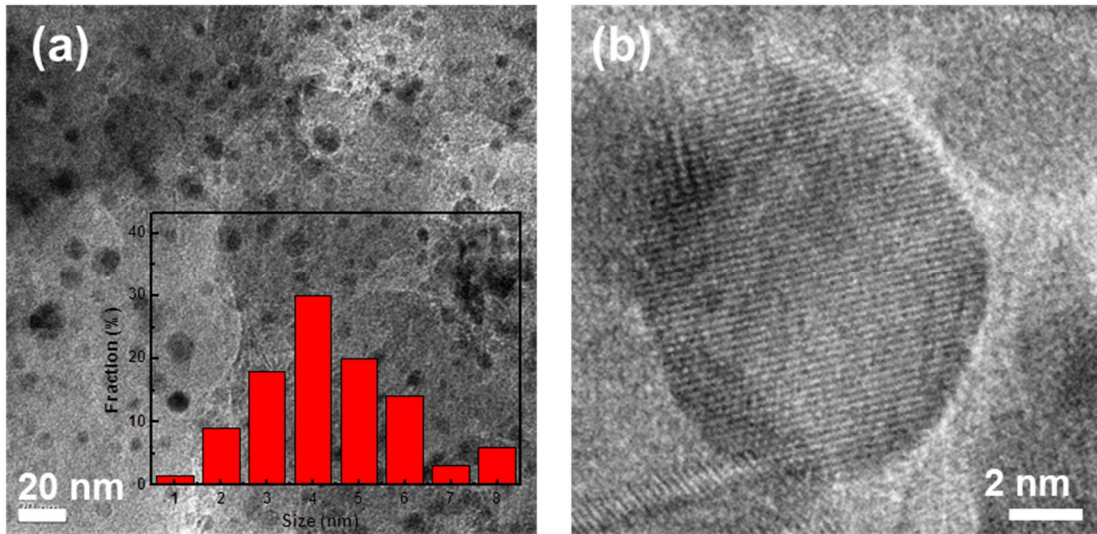


Figure 9 (a) TEM and (b) HRTEM images of GQDs, respectively. The inset in (a) shows the size distributions of GQDs.

XPS measurement was employed to exam the chemical composition of the GQDs. The XPS survey scan of GQDs (Figure 10a) shows a predominant graphitic C 1s peak at 284 eV, N 1s peak at 400 eV, and O 1s peak at 532 eV, indicating the incorporation of N atoms into GQDs due to the addition of ammonia. The high resolution C1s XPS spectrum of GQDs (Figure 10b) consists of four components at binding energies of 284.6 eV (sp^2 carbon C-C/C=C), 285.2 eV (C-N bond), 286.6 eV (sp^3 -carbon C-O), and 288.6 eV (C=O in carboxyl group). The UV-Vis absorption spectrum of the GQDs clearly shows a typical absorption peak located at 315 nm, and the GQDs strongly exhibit broad-band absorption in the UV region (Figure 11). These results indicate that the GQDs have strong absorptivity of UV light, giving them good UV sensitivity for optoelectronic applications.

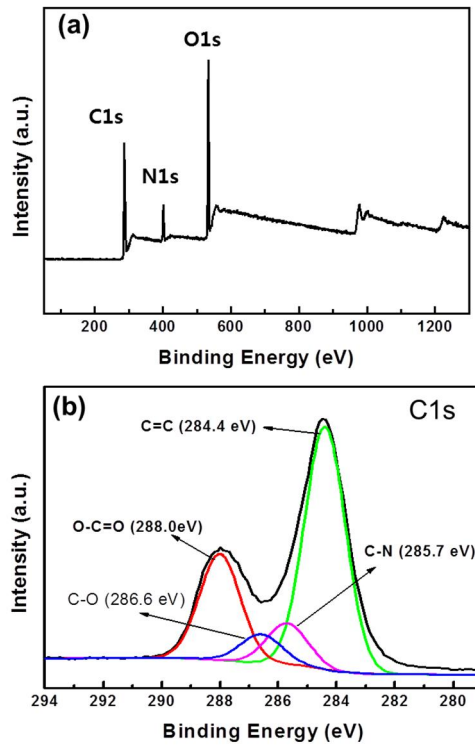


Figure 10 XPS spectra of the prepared GQDs: (a) the survey scan and (b) C1s core-level spectra.

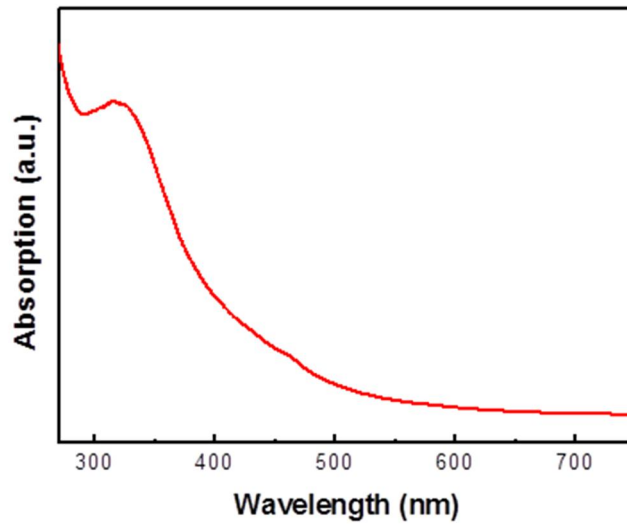


Figure 11 UV-Vis absorption spectra of GQDs.

To investigate the electrical interaction between GQDs and RGO, the I-V characteristics of GQDs/RGO hybrid under UV illumination of $20 \mu\text{W}/\text{cm}^2$ were measured by sweeping the bias voltage from -2 to 2 V at a 0.1 V scanning rate. As the control, the I-V curves of RGO film in Figure 12a show no detectable current change on UV illumination, indicating no photoresponse of RGO film. For the GQDs/RGO hybrids, the linear and symmetric I-V curves represent the Ohmic contact due to the strong interaction between GQDs and RGO. Importantly, the current from the GQDs/RGO hybrids increases on UV illumination and the resistance thus decreases from 4.90 to 2.84 k Ω (Figure 12b) by the integration of GQDs and RGO.

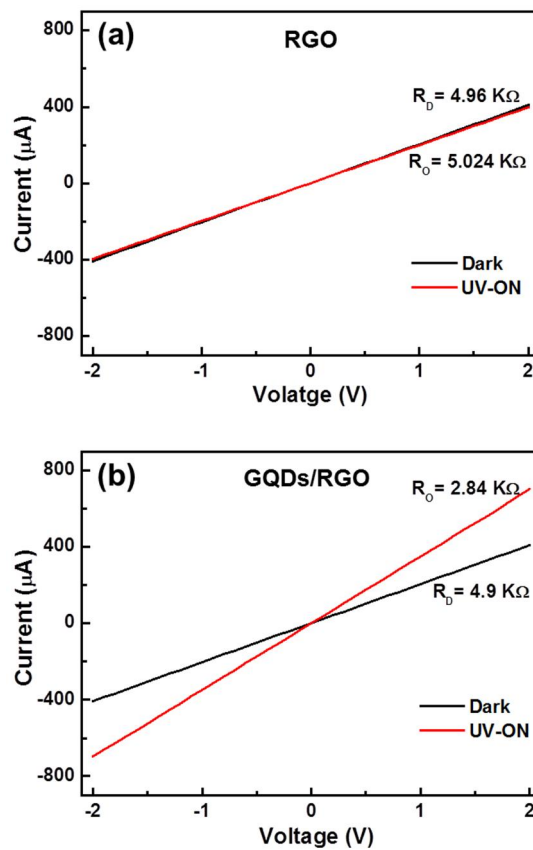


Figure 12 I-V curves of RGO (a) and GQDs/RGO (b) with and without the UV illumination of $20 \mu\text{W}/\text{cm}^2$.

We further investigated the time-resolved photoresponse of the GQDs/RGO hybrids under UV illumination of $20 \mu\text{W}/\text{cm}^2$ at a bias voltage of 2 V. As shown in Figure 13a, the UV sensor using GQDs/RGO hybrids demonstrates good photoresponse and repeatability. As the UV light is on, the current increases sharply and reaches the saturation value. When the light source is off, the current recovers to its initial value. It can be seen that the slight decrease of current occurred immediately after switching on the UV light, and the current then started increasing and reached the saturation regime. These results can be explained by the electron trapping of oxygen groups in RGO, resulting in the initial current decrease [14,15]. Furthermore, Figure 13b exhibits the time-dependent photo response of the GQDs/RGO hybrids under the various intensities of UV light at a bias voltage of 2 V. As expected, the saturation photocurrents increased along the increase of illumination intensities. Notably, the minimum detectable intensity of UV light was $0.4 \mu\text{W}/\text{cm}^2$ with a photocurrent of 0.42 mA and a low driving voltage, showing the good sensitivity of the hybrids sensor. The photo responsivity, which is defined as the photocurrent generated per unit power of incident light on the active area of the sensor device, is another important feature for the UV sensor. The photo responsivity (R) was determined by the expression $R = I_{\text{ph}}/P_o$, where I_{ph} is the photocurrent (A), and P_o is the incident optical power (W). Under the UV illumination of $20 \mu\text{W}/\text{cm}^2$, the photo responsivity of the device is calculated to be $8.7 \times 10^2 \text{ A/W}$, which is much higher than that of pristine graphene photo detectors [16] and other UV sensor based on ZnO [17,18]. In addition, the specific detectivity (D , Jones) represents the capability of the devices to detect a small photo signal and is determined by the expression $D = R/(2qI_0)^{1/2}$, where q is the absolute value of electronic charge (1.6×10^{-19} Coulombs) and I_0 is the dark current [18]. The specific detectivity of the hybrid UV sensor is determined to be 7.7×10^{13}

Jones under the UV light of $20 \mu\text{W}/\text{cm}^2$, which is comparable to that of the functional quantum dots/graphene hybrid photodetectors [20, 21]

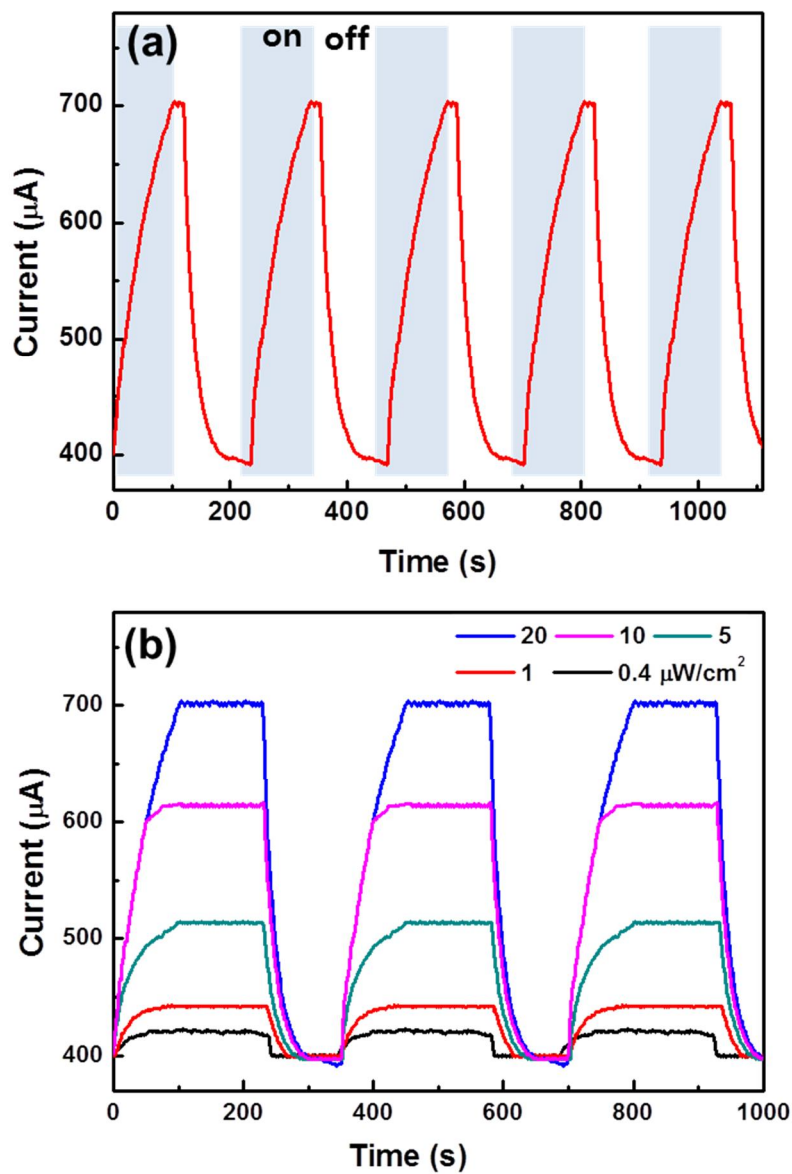


Figure 13 (a) Time-dependent photoresponse curves of the GQDs/RGO hybrid under the UV illumination of $20 \mu\text{W}/\text{cm}^2$. (b) Time-dependent photoresponse under the various UV light intensities.

To understand the photo induced charge transfer dynamics between GQDs and RGO, the PL measurements of GQDs, RGO, and GQDs/RGO were performed with the excitation of a 325 nm laser at room temperature. As shown in Figure 14, a strong blue emission from GQDs was observed with a peak located at 420 nm, whereas no detectable emission was observed from RGO. The fluorescence intensity of GQDs was quenched for the GQDs/RGO hybrids, which directly involves the effective transfer of the photo generated charges from GQDs to RGO. This PL quenching behavior of GQDs in the presence of RGO is consistent with the photo response characterization of GQDs/RGO, resulting in the enhanced photocurrent under UV illumination. To demonstrate theoretically mechanism of charge transfer, the linear potential scan was carried out to determine energy levels of GQDs. From the cathodic and anodic scan results in Figure 15, EHOMO and ELUMO of GQDs were calculated approximately to be -3.76 eV and -6.85 eV, respectively, and the calculated E_g of GQDs was 3.1 eV. Since the work function of RGO film is known to be about -4.5 eV [22,23], the higher position of ELUMO of GQDs than the work function of RGO film suggests the suitable electron transfer from GQDs to RGO. The corresponding electron transfer between GQDs and RGO film is illustrated in Figure 16, the electrons of GQDs are excited to the conduction band under UV light illumination, and the photo generated electrons transfer to the RGO film at the GQDs/RGO junction and flow through RGO to the Au electrode. Therefore, the recombination of photo generated electron-hole pairs is reduced and the photocurrent of devices is enhanced. These findings show that the NGQDs serve as excellent UV absorbing and charge generation materials and RGO functions as a charge transporting conductive material.

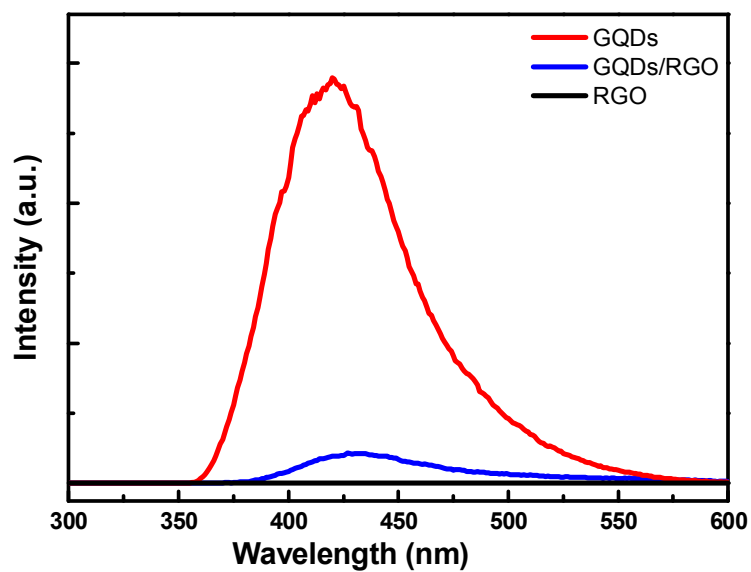


Figure 14 Photoluminescence spectra of RGO, GQDs, and GQDs/RGO hybrids.

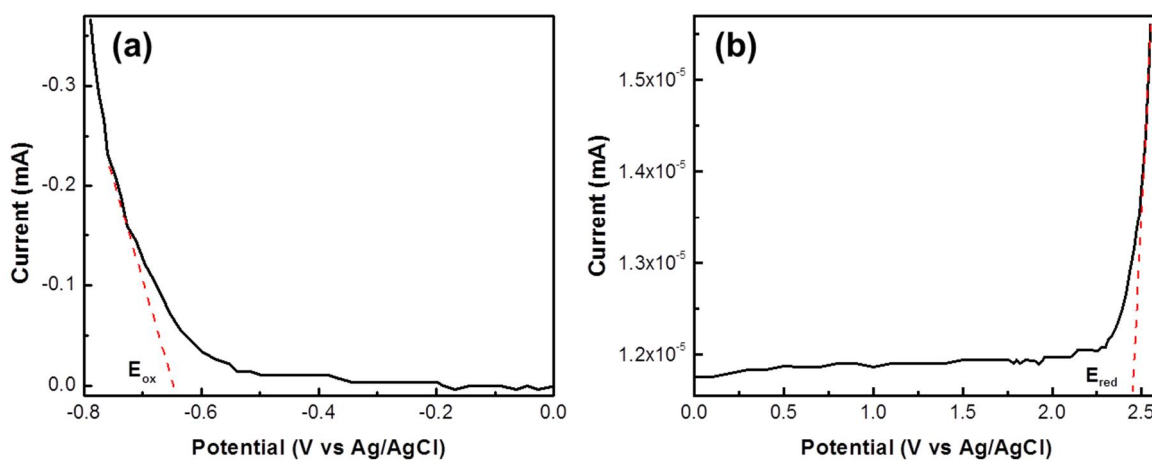


Figure 15 (a) Cathodic scan and (b) anodic scan of GQDs at 5mVs^{-1}

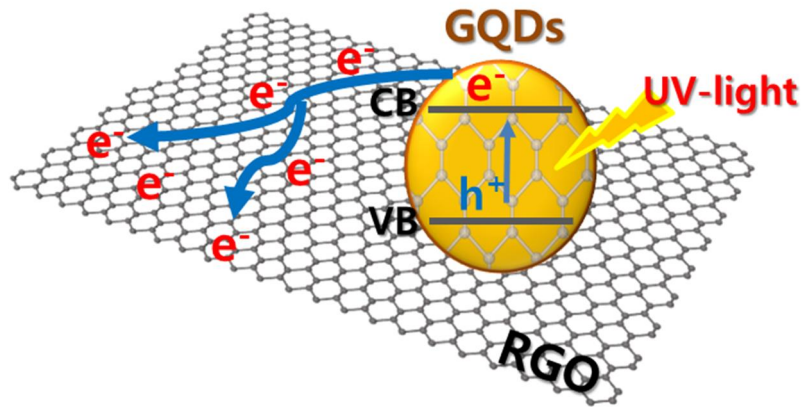


Figure 16 A schematic illustration of the mechanism for the enhanced performance of the GQDs/RGO hybrids UV sensor

3.4 Conclusion

We demonstrated the UV sensor based on GQDs/RGO hybrids using a simple and inexpensive solution-process, which exhibits an excellent sensing performance at a low operating voltage. Under UV light illumination of $20 \mu\text{W}/\text{cm}^2$, the GQDs/RGO hybrids sensor shows the large photo responsibility of $8.7 \times 10^2 \text{ A/W}$ and the high specific detectivity of $7.7 \times 10^{13} \text{ Jones}$. These high performances of the hybrids UV sensor are attributed to the strong absorption of UV light in GQDs, an efficient charge transfer at the GQDs/RGO junction, and a high electron mobility of RGO. Our novel approach based on the solution-processed UV sensor using all carbon materials suggests an alternative strategy for designing the promising optoelectronic applications.

Reference

- [1]. A.A. Balandin, S. Ghosh, W. Bao, I. Calizo, D. Teweldebrhan, F. Miao, C.N. Lau, Superior thermal conductivity of single-layer graphene, *Nano Lett.* 8 (2008) 902-907.
- [2]. C. Lee, X. Wei, J.W. Kysar, J. Hone, Measurement of the elastic properties and intrinsic strength of monolayer graphene, *Science* 321 (2008) 385-388.
- [3]. V. Singh, D. Joung, L. Zhai, S. Das, S I. Khondaker, S. Seal, Graphene based materials: Past, present, and future, *Prog. Mater. Sci.* 56 (2011) 1178-1271.
- [4]. K.S. Novoselove, A.K. Geim, S.V. Morozov, D. Jaing, Y. Zhang, S.V. Dubonos, I.V. Grigorieva, A. A. Firsov, Electric field effect in atomically thin carbon films, *Science* 306 (2004) 666-669.
- [5]. S. N. Baker, G. A. Baker, Luminescent carbon nanodots: Emergent nanolights, *Angew. Chem. Int. Ed.* 49(2010) 6726-6744.
- [6]. D. Qu, M. Zheng, L. Zhang, H. Zhao, Z. Xie, X. Jing, R.E. Haddad, H.Fan, Z.Sun, Formation mechanism and optimization of highly luminescent doped graphene quantum dots, *Sci. Rep.* 4(2014) 5294.
- [7]. H. Sun, L. Wu, W. Wei, X. Qu, Recent advances in graphene quantum dots for sensing, *Mater. Today* 16 (2013) 433-442.
- [8]. Li, G. Wu, G. Yang, J. Peng, J. Zhao, J.J. Zhu, Focusing on luminescent graphene quantum dots: current status and future perspectives, *Nanoscale* 5 (2013) 4015-4039.
- [9]. J. K. Wassei, R. B. Kaner, Graphene, a promising transparent conductor, *Mater. Today* 13 (2010), 52–59.

- [10]. V.H. Luan, H.N. Tien, L.T. Hoa, N.T.M. Hien, E.S. Oh, J.S. Chung, E.J. Kim, W.M. Choi, B.S. Kong, S.H. Hur, Synthesis of a highly conductive and large surface area graphene oxide hydrogel and its use in a supercapacitor, *J. Mater. Chem. A* 1 (2013), 208–211.
- [11]. T.V. Tam, N.B. Trung, H.R. Kim, J.S. Chung, W.M. Choi, One-pot synthesis of N-doped graphene quantum dots as a fluorescent sensing platform for Fe³⁺ ions detection, *Sensor. Actuat. B: Chem.* 202 (2014) 586-573.
- [12]. L. R. Radovic, B. Bockrath, On the chemical nature of graphene edges: Origin of stability and potential for magnetism in carbon materials, *J. Am. Chem. Soc.* 127 (2005) 5917–5927.
- [13]. K. A. Mkhoyan, A. W. Contryman, J. Silcox, D. A. Stewart, G. Eda, C. Mattevi, S. Miller, M. Chhowalla, Atomic and electronic structure of graphene-oxide, *Nano Lett.* 9 (2003) 1058-1063.
- [14]. B. Chitara, S. B. Krupanidhi, C. N. R. Rao, Solution processed reduced graphene oxide ultraviolet detector, *Appl. Phys. Lett.* 99 (2011) 113114.
- [15]. H. Chang, Z. Sun, Q. Yuan, F. Ding, X. Tao, F. Yan, Z. Zheng, Thin film field-effect phototransistors from bandgap-tunable, solution-processed, few-layer reduced graphene oxide films, *Adv. Mater.* 22 (2010) 4872-4876.
- [16]. F. Xia, T. Muller, Y.M. Lin, A. V. Garcia, P. Avouris, Ultrafast graphene photodetector, *Nat. Nanotechnol.* 4 (2009) 839-843.
- [17]. Y. K. Su, S. M. Peng, L. W. Ji, C. Z. Wu, W. B. Cheng, C. H. Lui, Ultraviolet ZnO nanorod photosensors, *Langmuir* 26 (2010) 603-606.

- [18]. Z. Wang, X. Zhan, Y. Wang, S. Muhammad, Y. Huang, J. He, A flexible UV nanosensor based on reduced graphene oxide decorated ZnO nanostructures, *Nanoscale* 4 (2012) 2678-2684.
- [19]. G. Konstantatos, I. Howard, A. Fischer, S. Hoogland, J. Clifford, E. Klem, L. Levina, E. Sargent, Ultrasensitive solution-cast quantum dot photodetectors, *Nature* 442 (2006) 180-183.
- [20]. G. Konstantatos, M. Badioli, L. Gaudreau, J. Osmond, M. Bernechea, F. P. G. Arquer, F. Gatti, F. H. L. Koppens, Hybrid graphene–quantum dot phototransistors with ultrahigh gain, *Nat. Nanotechnol.* 7 (2012) 363-368.
- [21]. K. K. Manga, J. Wang, M. Lin, J. Zhang, M. Nesladek, V. Nalla, W. Ji, K. P. Loh, Highperformance broadband photodetector using solution-processible PbSe–TiO₂–graphene hybrids, *Adv. Mater.* 24 (2012) 1697-1702.
- [22]. P. Yu, X. Wen, Y. R. Toh, Y. C. Lee, K. Y. Huang, S. Huang, S. Shertha, G. Conibeer, J. Tang, Efficient electron transfer in carbon nanodot-graphene oxide nanocomposites, *J. Mater. Chem. C* 2 (2014) 2894-2901.
- [23]. V. Gupta, N. Chaudhary, R. Srivastava, G. D. Sharma, R. Bhardwaj, S. Chand, Luminescent graphene quantum dots for organic photovoltaic devices, *J. Am. Chem. Soc.* 133 (2011) 9960-9963.

CHAPTER 4: Facile synthesis of cysteine-functionalized graphene quantum dots for a fluorescence probe toward mercury ions

4.1 Introduction

Graphene, a one-atom-thick planar sheet of sp²-hybridized carbon atoms packed in a honeycomb lattice, is now a promising material for various applications [1-4]. Among graphene-based materials, graphene quantum dots (GQDs), the zero-dimensional form of graphene with diameters below 100 nm, have attracted growing research interest for their tunable electronic and opto-electronic properties, which are directly associated with quantum confinement and chemical functionalization. In comparison with the traditional semiconductor quantum dots, GQDs possess excellent characteristics such as high photoluminescent activity, stable fluorescence without photobleaching, biocompatibility, and low toxicity [5-7]. Many efforts have been made in their preparation and tremendous synthetic methods developed. Generally, GQDs can be produced using top-down or bottom-up approaches. The former approach involves the decomposition of carbon-based materials, including carbon nanotube, carbon fiber and graphene oxide, using physical or chemical treatments [8-12]. The time-consuming oxidative-cutting method is typically used to synthesize GQDs, which are of non-uniform size and low production yield. By contrast, the bottom-up strategy has been developed using small cyclic molecules by the hydrothermal process or high-temperature pyrolysis with easy control of lateral size [13, 14]. This approach, however, results in poor quality GQDs and a complicated synthesis process. The covalent functionalization of GQDs is a strategy to tailor their electronic, chemical, physiochemical and photophysical properties. Up to now, few studies have focused on covalent

functionalization of GQDs, and thereported processes require many complicated purification steps [15, 16]. In this regard, the development of the simple functionalization of GQDs remains highly desirable.

Due to strong toxicity and bioaccumulation of heavy metal ions, it is important to develop novel and rapid detection methods with high sensitivity for their detection. Among the various sensing methods, fluorescence sensing approaches have been utilized for the detection of metals because of their excellent sensitivity, fast response, ease of operation and ability to detect in a non-destructive manner. Semiconductor quantum dots (QDs) are widely used for the fluorescence probe owing to their high quantum yield, wide light-absorption band, and size-tunable emission profiles [17, 18]. As a new class of sensor materials, fluorescence probes of GQDs have been reported on in various studies, due to their excellent optical properties, biocompatibility, and good solubility in polar and non-polar solvents [19, 20]. These characteristics make GQDs-based advanced fluorescent sensors potentially promising for highly sensitive and selective detection of heavy metal ions. In this work we report a facile, green and simple strategy for the synthesis of cysteine functionalized GQDs (cys-GQDs). Using the method proposed here, cys-GQDs are synthesized with a uniform lateral size distribution and a strong green photoluminescence with a high quantum yield. The obtained cys-GQDs are employed for the specific detection of Hg^{2+} , which exhibits a highly sensitive and selective fluorescent sensor for Hg^{2+} detection even at low concentrations.

4.2 Experiment

4.2.1 Synthesis of cys-GQDs

The synthesis of GQDs was prepared by the method described in our previous report.²⁰ Typically, citric acid (CA, 3.2 g) and distilled water (80 ml) were mixed by constant stirring at room temperature for 30 minutes, followed by sonication for 30 minutes to form a clear solution. After the solution was adjusted to pH 10 by using potassium hydroxide, it was transferred into a 150 ml Teflon-lined stainless autoclave. The autoclave was sealed and heated to 160°C in an oven for 4 hours, and the resultant yellow solution was cooled to room temperature. L-cysteine was added into the yellow solution with constant stirring for 30 min, and the mixture was refluxed at 80°C for 24 hours. Subsequently, the mixture solution was dialyzed using a dialysis bag (3,000 Da, Spectrum Lab. Inc) for two days to remove potassium hydroxide and small impurities. Finally, a light yellow solution of cys-GQDs was obtained. For the characterizations, the samples of cys-GQDs were prepared by adding 0.8 wt% of L-cysteine in the functionalization process.

4.2.2 Characterizations

The nanostructures of cys-GQDs were examined with a high resolution transmission electron microscope (HR-TEM, JEM-2100F, JEOL) and atomic force microscopy (AFM; Veeco, Dimension 3100) in tapping mode. X-ray photoelectron spectroscopy (XPS; Thermo Fisher) measurements were performed using monochromatic AlK α radiation ($h\nu = 1486.6$ eV). UV-visible absorption spectra were recorded with a Bruker Avance 400 spectrometer (400.13 MHz) and Specord 210 UV-vis spectrophotometer, respectively. Raman spectroscopy (DXR Raman spectrometer, Thermo Scientific) was acquired from 1,000 to 2,000 cm⁻¹ at room temperature with a 532 nm excitation source, and Fourier transform

infrared (FT-IR, Nicolet IR 200 spectrometer, Thermo Scientific) spectra were measured to verify the functional groups. Fluorescence spectroscopy (Cary Eclipse Fluorescence Spectrophotometer, Agilent) and time-resolved fluorescence (Spex Fluorolog-3, Horiaba) were performed at room temperature. For the Hg²⁺ detection experiments, 1 ml of cys-GQDs solution (0.03 mg/ml) was prepared and mixed with 1 ml solutions of the different Hg²⁺ concentrations. The mixture was left for 5 minutes at room temperature, followed by fluorescence spectra measurements with the excitation wavelength of 420 nm. Furthermore, detection experiments of various metal ions were performed using various metal ion sources, such as Hg(NO₃)₂, Pb(NO₃)₂, Cd(NO₃)₂·4H₂O, NaCl, KCl, Fe(NO₃)₃·9H₂O, Mn(NO₃)₂·xH₂O, Cr(NO₃)₃·9H₂O, Zn(NO₃)₂, LiNO₃, Cu(NO₃)₂, and AgNO₃. A 1 ml metal ion solution was added to 1.0 ml of cys-GQDs solution (0.03 mg/ml) with retention for 5 minutes, and then the fluorescence spectra were recorded with the excitation wavelength of 420 nm. The fluorescence quenching efficiency of cys-GQDs can be well described by the following Stern-Volmer equation:

$$\frac{F_0}{F} - 1 = K_{sv}[Q]$$

where F_0 and F are the fluorescence intensities of cys-GQDs in the absence and presence of metal ions, K_{sv} is the Stern-Volmer quenching constant and $[Q]$ is the concentration of metal ions.

4.3 Results and discussions

Fig. 17a shows a schematic of the preparation of cys-GQDs comprising the synthesis of GQDs using CA and the functionalization of GQDs with L-cysteine as precursors. First, CA is carbonized and converted into small graphitic dots by the hydrothermal process at high

temperature. During the hydrothermal process, the graphitic dots undergo diffusion and condensation to form crystalline GQDs, containing oxygen functional groups (carboxylic and epoxide) at the basal plane and the edge. Then, the synthesized GQDs are simultaneously functionalized using L-cysteine in the base environment through the amidation reaction which occurs between NH_2 of L-cysteine and the oxygen functionalities of GQDs [21]. The TEM image of the prepared cys-GQDs in Fig. 17b reveals a fairly uniform size distribution of samples with an average lateral diameter of 3.8 nm. In addition, the graphitic lattice of GQDs can be clearly observed in the HR-TEM image (the inset of Fig.17b). The observed lattice spacing of 0.25 nm corresponds to the hexagonal lattice plane spacing of d_{1120} [9], indicating that the synthesized cys-GQDs are of high crystallinity. The AFM results (Fig. 18) reveal that the average height of the cys-GQDs is about 1.25 nm, suggesting that they are mostly single-layered [10, 22].

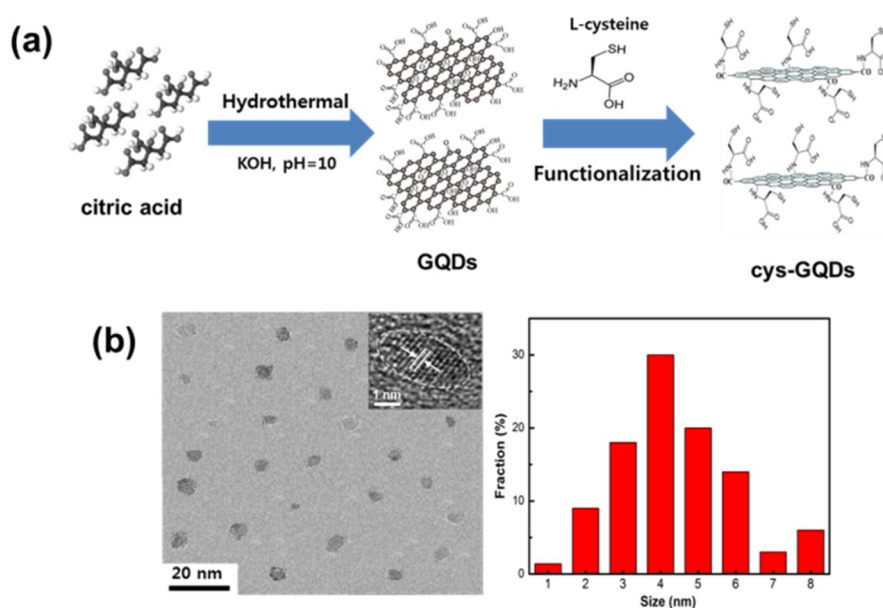


Figure 17 (a) Schematic illustration of the synthesis of cys-GQDs. (b) TEM images of the synthesized cys-GQDs and their size distribution.

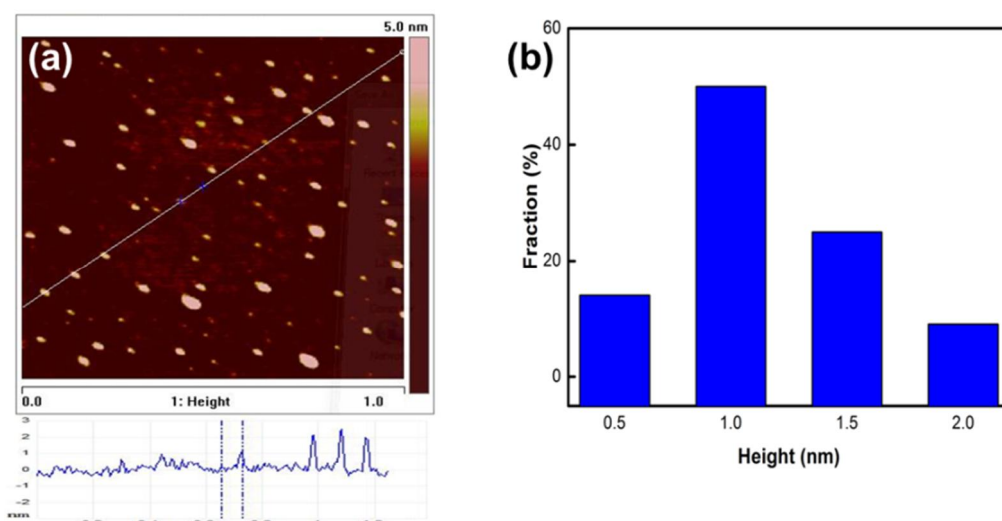


Figure 18 (a) AFM image and (b) the height distributions of cys-GQDs.

XPS measurements were performed to investigate the atomic composition and chemical bonding of the cys-GQDs and presented in Fig.19. While the wide scan survey XPS spectrum of pristine GQDs shows only two peaks, of C1s at 284 eV and O1s at 532 eV, the wide scan spectrum of cys-GQDs exhibits two new peaks, of N1s and S2p at 399.8 and 167 eV, respectively, as evidence of the functionalization of GQDs by L-cysteine (Fig. 19a). The strong C1s peak corresponding to sp^2 carbon indicates that the conjugated bonds in graphene lattice are retained after the functionalization. Compared to the pristine GQDs, the O1s peak intensity of the cys-GQDs decreases, which indicates that the reduction of oxygen functionalities in GQDs occurs by the functionalization by L-cysteine. The high-resolution C1s spectrum of cys-GQDs (Fig. 19b) is deconvoluted into six components, corresponding to C=C (284.5 eV), sp^3 carbon (285.4 eV), C-N (286.3 eV), C-S/C-O (287.6 eV), C=O (288.2 eV) and O-C=O (289 eV). However, the C-N bond peak is observed due to the amine groups of L-cysteine on the cys-GQDs surface. The high resolution N1s spectrum of cys-GQDs (Fig.

19c) shows a clear peak of the pyrrolic N(C-NH-C) at 399.4 eV. The higher resolution S2p spectrum (Fig. 19d) shows an S2p_{3/2} peak at 163.3 eV, assigned to the thiol group (S-H) of L-cysteine molecules. The other peaks at 165.12, 167.78 and 168.19 eV may be attributed to the phenomenon of spin orbit separation. These results suggest that the cys-GQDs are synthesized by the amidation reaction between the amine groups of L-cysteine and the carboxylic groups of GQDs. The FT-IR and Raman characterization of pristine GQDs and cys-GQDs are further performed to confirm the synthesis of cys-GQDs. In the FT-IR spectra (Fig. 20a), the pristine GQDs have a broad O-H stretching peak at 3400 cm⁻¹, a C=C stretching peak at 1623 cm⁻¹, and a C-O stretching peak in the carboxylic groups at 1398 cm⁻¹. The cys-GQDs exhibit new absorption peaks at 3340, 2870, 1725, and 1250 cm⁻¹, corresponding to N-H bending, S-H stretching peak, C-N stretching vibration, and C=O absorption, whose functional groups are formed after the functionalization. These results clearly confirm that L-cysteine is covalently bonded to the surface of GQDs, which is consistent with the XPS results. Raman spectra were measured to further confirm the quality of the prepared cys-GQDs. Raman spectra of pristine GQDs and cys-GQDs (Fig. 20b) show that the pristine GQDs and the cys-GQDs both have two dominant peaks, which are G peak at around 1600 cm⁻¹, related to the in-plane vibration of the sp² carbon lattice, and a D peak at around 1360 cm⁻¹, related to the presence of sp³ structural defects. Compared to the pristine GQDs, the cys-GQDs exhibit significant red shifts of both G and D peaks. The G and D peaks shift from 1607 to 1584 cm⁻¹ and from 1355 to 1342 cm⁻¹, respectively. The red shift of Raman spectra for the cys-GQDs could be explained by the functionalization of L-cysteine molecules on the surface of GQDs [21, 23, 24]. Furthermore, the ratio of the intensities of the

D and G peaks (I_G/I_D) is 1.09 for the pristine GQDs and 1.06 for the cys-GQDs, showing that both the pristine GQDs and the cys-GQDs are highly crystalline.

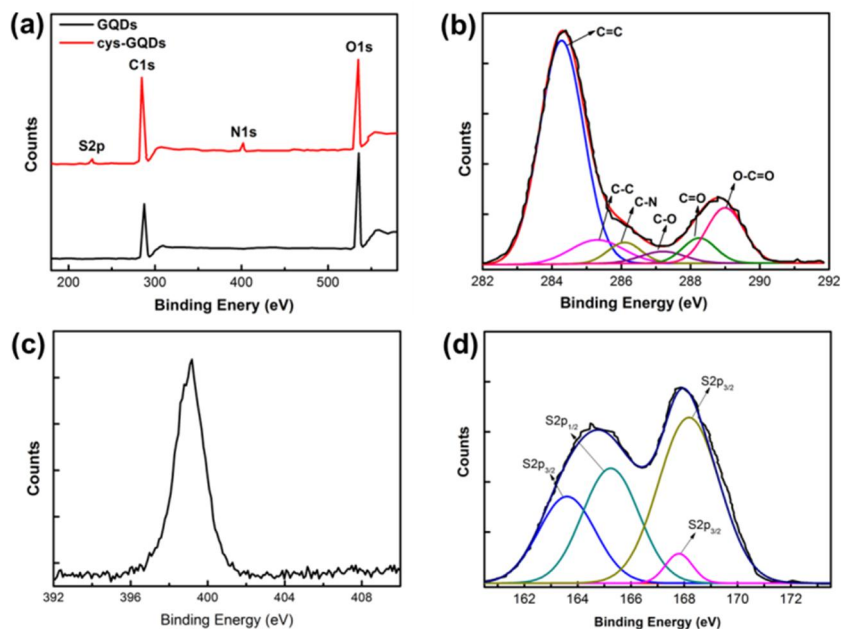


Figure 19 XPS survey scan of as-prepared GQDs and cys-GQDs. (b) C1s, (c) N1s and (d) S2p core-level XPS spectra of cys-GQDs.

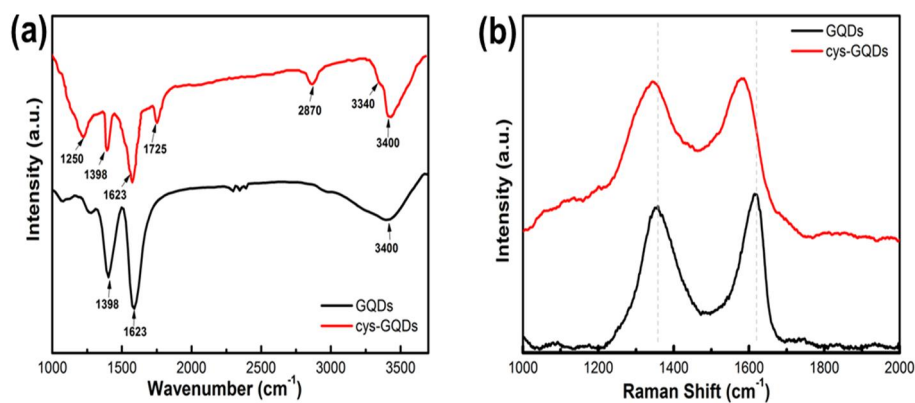


Figure 20 (a) FT-IR Spectroscopy and (b) Raman Spectroscopy of as-produced GQDs and cys-GQDs.

To analyze the optical properties of cys-GQDs, we performed UV-Vis absorption and PL analysis of the prepared cys-GQDs aqueous solution. The UV-Vis absorption spectrum of the pristine GQDs (Fig. 21a) exhibits a strong peak at 321 nm and a shoulder at 452 nm, corresponding to the electron transitions from π to π^* of C=C and C=O bonds. However, the UV-Vis spectrum of cys-GQDs shows a clear shift of the two absorption peaks to 331 and 503 nm after the functionalization of GQDs with L-cysteine [25]. The PL emission spectra of the obtained cys-GQDs with the various concentrations of L-cysteine when excited at 365 nm are presented in Fig. 21b. However, the emission peak of the pristine GQDs is observed at 460 nm, the emission peak of the cys-GQDs demonstrates a red-shifted with increases in the L-cysteine concentration. The wavelength at the emission peak is shifted from 485 to 532 nm when the concentration of L-cysteine increases from 0.2 to 0.8 wt%, demonstrating the tunable fluorescence of cys-GQDs. In addition, the strong orbital interaction between the amine group and the π -conjugated system of functionalized GQDs can lift the degenerate HOMO orbitals to higher energy, which could explain the red shift of PL spectra. Fig.21c shows the excitation wavelength-dependent PL spectra of the cys-GQDs (0.8 wt% of L-cysteine) when excited in a range from 400 to 500 nm. The emission peaks shift from 530 nm to 545 nm and, remarkably, their intensities decrease. These results are attributed to the optical selection for the different sizes and the surface defects of GQDs, which was extensively reported with the fluorescent carbon-based nano materials [22]. The quantum yield of cys-GQDs (Table 1) is determined to be around 28% using quinine sulphate as a standard reference (54% in 0.5 M H₂SO₄), which is much higher than that of the pristine GQDs (8.8%). The higher quantum yield of the cys-GQDs could be attributed to L-cysteine boned on the GQDs surfaces which bears the electron-donating amine groups [26].

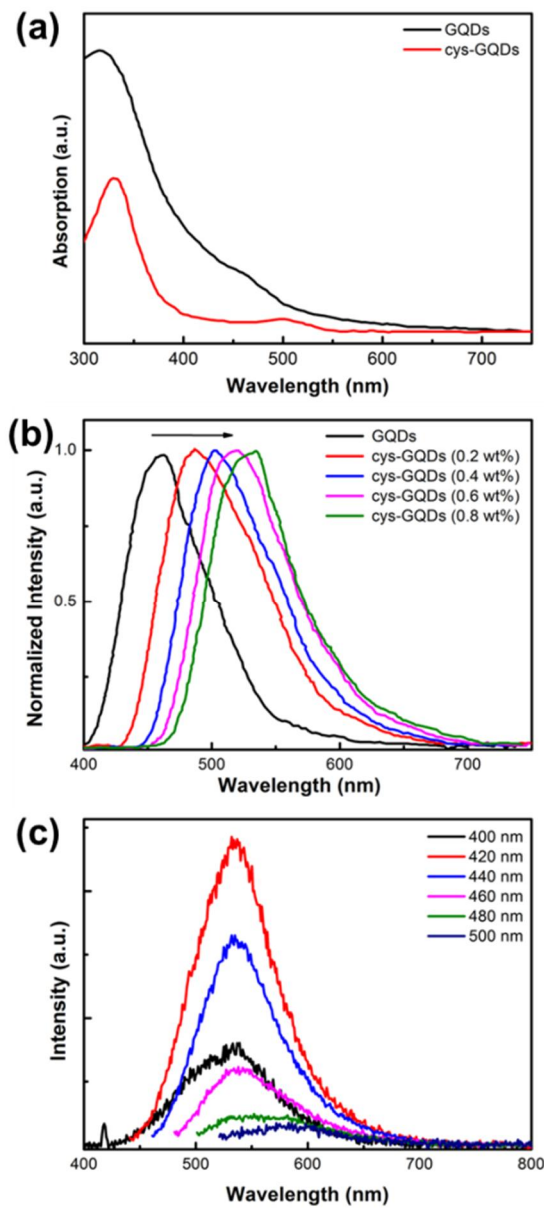


Figure 21 Spectra of (a) UV-vis adsorption of GQDs and cys-GQDs. (b) Photoluminescence spectra of cys-GQDs with various amounts of L-cysteine. (c) The fluorescence spectra of cyst-GQDs at different excitation wavelengths ranging from 400 nm to 500 nm.

Table 1. The quantum yield of GQDs and cys-GQDs

Sample	Emission intensity (I)	Absorption (A)	Refractive index (n)	Quantum yield (Q)
Quinine sulfate	30110	1.5906	1.33	0.54
cys-GQDs	6073	0.62515	1.33	0.28
GQDs	4523	1.4675	1.33	0.088

To evaluate the fluorescent probe application, the fluorescence changes of cys-GQDs (0.8 wt% of L-cysteine) were measured in the presence of various metal ions at the same concentration of 100 μM (Fig.22a). Impressively, whereas other metal ions exhibit negligible change of fluorescence, the addition of Hg^{2+} causes the significant fluorescence quenching of cys-GQDs to decrease by about 75%, which shows that the fluorescence quenching of cys-GQDs is highly selective for Hg^{2+} . In addition, it can be clearly observed that the green fluorescence of cys-GQDs with irradiation of 365 nm UV light quenched upon the addition of Hg^{2+} (Fig.22b). To explore the Hg^{2+} detection sensitivity of cys-GQDs, with varying concentrations of Hg^{2+} from 1 μM to 500 μM , the fluorescence changes of cys-GQDs were measured. As shown in Fig.22c, the fluorescence intensities gradually decreases with increasing concentrations of Hg^{2+} , and the spectral maximum peaks are retained at around 530 nm. The Hg^{2+} concentration dependent fluorescence (Fig.22d) shows the drastic quenching from the low concentration to 100 μM , and the saturated change in the higher concentrations. The maximum fluorescence quenching of 92% is observed with an Hg^{2+} concentration of 500 μM . A Stern-Volmer plot in the range of 0-10 μM shows a linear behavior, having the correlation coefficient $R^2= 0.9978$ (inset of Fig. 22d). The calculated

Stern-Volmer constant, KSV, is found to be $3.4 \times 10^{-7} \text{ M}^{-1}$. This value is higher than that of quenching between simple organic dyes/quencher pairs [27], indicating efficient fluorescence quenching by the cys-GQDs and Hg^{2+} pairs. The detection limit calculated following the 3σ IUPAC criteria is $0.02 \mu\text{M}$ which is lower than that of previously reported fluorescence probes [28, 29, 30].

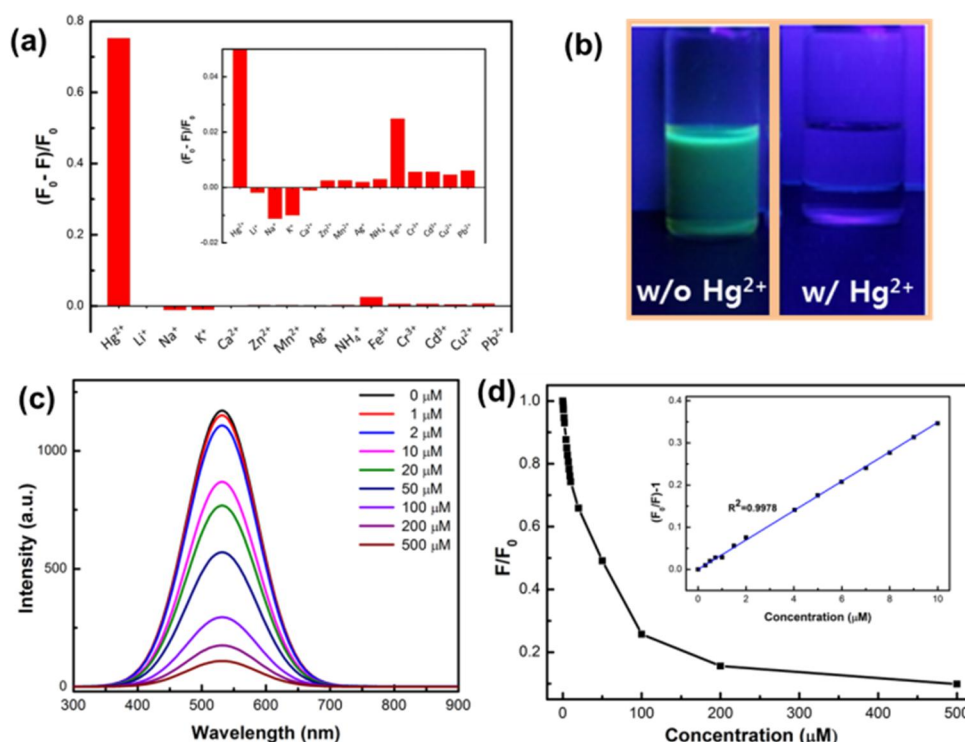


Figure 22 (a) The fluorescence enhancement factors $[(F-F_0)/F_0]$ of cys-GQDs for the various metal ions ($100.0 \mu\text{M}$). (b) The photo images of the cys-GQDs solutions in the presence (right) and absence of Hg^{2+} (left) under the 365nm UV light irradiation. (c) The fluorescence change of cys-GQDs with the various Hg^{2+} concentrations. (d) The dependence of F/F_0 on the concentration of Hg^{2+} in the range of 0-500 μM . The inset shows a Stern-Volmer plot for the fluorescence quenching of cys-GQDs with the range of 0-10 μM .

To investigate the applicability of the proposed method for analyzing Hg^{2+} in real samples, the practicality of the assay was examined by testing Hg^{2+} in real water. For this purpose, a water samples used for quantitative analysis was collected from the Taehwa River in Ulsan city, South of Korea. The sample was first filtered by 0.25 μm membrane and centrifuged at 100000 rpm for 20 minutes to remove any suspended particles. A series of samples was prepared by adding standard solutions containing various concentrations of Hg^{2+} ion in 80 μL Tris-HCl buffer (10 mM, pH 8.0) into the river water. The obtained solutions were further mixed with cys-GQDs solutions (0.003 mg/ML, 10 μL). The fluorescence was recorded under excitation of 410 nm and no fluorescence quenching was observed for pretreated river sample. As shown in table 2, the recoveries were found to be in the range from of 92.48 to 99.06 % and the relative standard deviation (RSD, n=5) was less than 4%. In spite of the possible interference from mineral and organic species existing in river water, the sensing system can still detect Hg^{2+} efficiently. These results indicate that the proposed method has the excellent applicability and reliability for Hg^{2+} detection.

Table 2. Determination results of Hg^{2+} in river water samples

Samples	Added (μM)	Found (μM)	RSD (% , n=5)	Recovery (%)
1	0.3	0.2972	3.6	99.06
2	0.5	0.4986	4.0	99.72
3	0.7	0.6905	2.9	98.64
4	1	0.9248	3.4	92.48

For the fluorescence quenching mechanism of cys-GQDs in the presence of Hg^{2+} , the FT-IR spectroscopy was taken to study the chemical interaction between the cys-GQDs and Hg^{2+} . Fig. 23a presents the FT-IR spectra change of cys-GQDs upon the addition of 40 μM Hg^{2+} . The peak at 2552 cm^{-1} assigned to the S-H vibration of the thiol group of cys-GQDs almost disappears in the presence of Hg^{2+} , which may be attributed to the formation of S-Hg bonding by the deprotonation of the thiol group. Furthermore, the symmetric COO^- stretching band at 1421 cm^{-1} shifts to the lower wavelength due to the bonding interaction between Hg^{2+} and the COO^- group of cys-GQDs. These results confirm the chemical bond formation between Hg^{2+} and the cys-GQDs. The time-resolved fluorescence spectroscopy was further carried out to explore the Hg^{2+} induced fluorescence quenching mechanism of the cys-GQDs. Fig. 23b shows the fluorescence decay of the cys-GQDs in the absence and presence of Hg^{2+} (40 μM). The fluorescence lifetime of the cys-GQDs in the absence of Hg^{2+} is found to be 7.2 ns with the excitation wavelength of 446 nm and the emission of 538 nm, indicating an excitation and recombination process of the cys-GQDs. Upon the addition of Hg^{2+} ion, the lifetime of the cys-GQDs decreases to 5.1 ns. Based on previous reports [31, 32], the lifetime of carbon-based quantum dots decrease because a electron acceptor or surface modifier adsorbs onto quantum dots surface. It suggests that the dynamic fluorescent quenching occurs through a fast electron transfer between the cys-GQDs and Hg^{2+} . By the complex formation between the cys-GQDs and Hg^{2+} , the radiative recombination of excitons is constrained through an effective electron transfer process from the cys-GQD to Hg^{2+} , resulting in a remarkable fluorescence quenching as depicted in Fig. 21c.

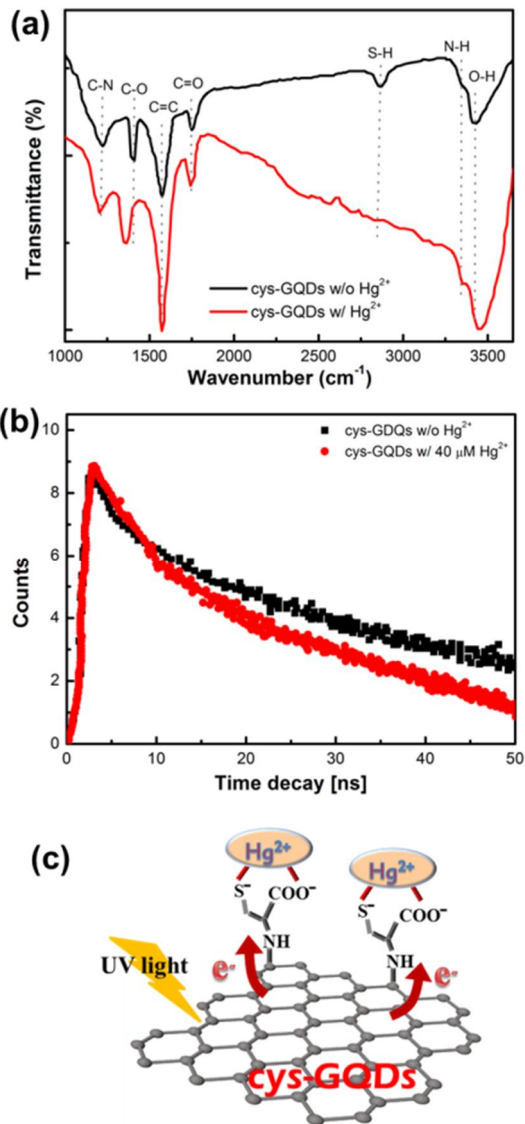


Figure 23 FT-IR spectra of cys-GQDs in the presence and absence of Hg²⁺. **(b)** Fluorescence decay of cys-GQDs as the function of time in the presence of Hg²⁺. **(c)** Schematic presentation of the fluorescence quenching mechanism of cys-GQDs in the presence of Hg²⁺.

4.4 Conclusion

In conclusion, we have demonstrated the synthesis of cys-GQDs by a simple and facile process, which involves the carbonization of CA and the functionalization of L-cysteine through a hydrothermal process. The as-prepared cys-GQDs have a green fluorescence under UV irradiation and high crystallinity with uniform size distribution. It is further found that the cys-GQDs exhibit tunable fluorescence by tuning the amount of L-cysteine, which is attributed to a π -conjugated interaction between GQDs and the amine group of L-cysteine. Furthermore, the cys-GQDs show their suitability as a highly sensitive and selective fluorescent probe for Hg^{2+} detection. The significant fluorescence quenching of cys-GQDs occurs in the presence of Hg^{2+} through the electron transfer process by the complex formation of cys-GQDs and Hg^{2+} . It is believed that the present work would pave the way for promising applications such as fluorescence probes, bio-sensors, and bio-medical imaging.

Reference

- [1]. K. S. Novoselov, A. K. Geim, S. V. Morozov, D. Jiang, Y. Zhang, S. V. Dubonos, I. V. Grigorieva and A. A. Firsov, *Science*, 2004, 306, 666.
- [2]. A.K. Geim and K. S Novoselov, *Nat. Mater.*, 2007, 6, 183.
- [3]. D. R. Dreyer, R. S. Ruoff and C. W. Bielawski, *Angew. Chem. Int. Ed.*, 2010, 49, 9336.
- [4]. Ch. K. Chua and M. Pumera, *Chem. Soc. Rev.*, 2013, 42, 3222.
- [5]. L. A. Ponomarenko, F. Schedin, M. I. Katsnelson, R. Yang, E.W. Hill, K. S. Novoselov and A. K. Geim, *Science*, 2008, 320, 356.

- [6]. L. Li, G. Wu, G. Yang, J. Peng, J. Zhao and J.-J. Zhu, *Nanoscale*, 2013, 5, 4015.
- [7]. S. H. Jin, D. H. Kim, G. H. Jun, S. H. Hong and S. Jeon, *ACS Nano*, 2013, 7, 1239.
- [8]. H. Tao, K. Yang, Z. Ma, J. Wan, Y. Zhang, Z. Kang and Z. Liu, *Small*, 2012, 8, 281.
- [9]. J. Peng, W. Gao, B. K. Gupta, Z. Liu, R. Romero-Aburto, L. Ge, L. Song, L. B. Alemany, X. Zhan, G. Gao, S. A. Vithayathil, B. A. Kaiparettu, A. A. Marti, T. Hayashi, J. J. Zhu and P. M. Ajayan, *Nano Lett.*, 2012, 12, 844.
- [10]. L. L. Li, J. Ji, R. Fei, C. Z. Wang, Q. Lu, J. R. Zhang, L. P. Jiang and J. J. Zhu, *Adv. Funct. Mater.*, 2012, 22, 2917.
- [11]. D. Y. Pan, J. C. Zhang, Z. Li and M. H. Wu, *Adv. Mater.*, 2010, 22, 734.
- [12]. K. Habiba, V. I. Makarov, J. Avalos, M. J. F. Guinel, B. R. Weiner and G. Morell, *Carbon*, 2013, 64, 341.
- [13]. J. Shen, Yi. Z. X. Yang and C. Li, *Chem. Commun.*, 2012, 48, 3686.
- [14]. C. K. Chua and M. Pumera, *Chem. Soc. Rev.*, 2014, 43, 291.
- [15]. R. Sekiya, Y. Uemura, H. Murakami and T. Haino, *Angew. Chem. Int. Ed.*, 2014, 53, 5725.
- [16]. A. Nahain, J. E. Lee, I. In, H. Lee, K. D. Lee, J. H. Jeong and S. Y. Park, *Mol. Pharmaceutics*, 2013, 10, 3736.
- [17]. Y. Chen and Z. Rosenzweig, *Anal. Chem.*, 2002, 74, 5132.
- [18]. A. M. Derfus, W. C. W. Chan and S. N. Bhatia, *Nano Lett.*, 2004, 4, 11.
- [19]. H. Sun, L. Wu, W. Wei and X. Qu, *Mater. Today*, 2013, 16, 433.

- [20]. T. V. Tam, N. B. Trung, H. R. Kim, J. S. Chung and W. M. Choi, *Sens. Actua. B*, 2014, 202, 568.
- [21]. S. Muralikrishna, K. Sureshkumar, Thomas S. Varley, D. H. Nagaraju and T. Ramakrishnappa, *Anal. Methods*, 2014, 6, 8698.
- [22]. S. Zhu, J. Zhang, Ch. Qiao, S. Tang, Y. Li, W. Yuan, B. Li, L. Tian, F. Liu, R. Hu, H. Gao, H. Wei, H. Zhang, H. Ch. Sun and B. Yang, *Chem. Commu.*, 2011, 47, 6858.
- [23]. V. Georgakilas, M. Otyepka, A. B. Bourlinos, V. Chandra, N. Kim, K. C. Kemp, P. Hobza, R. Zboril and K. S. Kim, *Chem. Rev.*, 2012, 112, 6156.
- [24]. N. H. Kim, T. Kuila and J. H. Lee, *J. Mater. Chem. A*, 2014, 2, 2681.
- [25]. Y. Lu, Y. Jiang, W. Wei, H. Wu, M. Liu, L. Niu and W. Chen, *J. Mater. Chem.*, 2012, 22, 2929.
- [26]. H. Tetsuka, R. Asahi, A. Nagoya, K. Okamoto, I. Tajima, R. Ohta and A. Okamoto, *Adv. Mater.*, 2012, 24, 5333.
- [27]. J. R. Lakowicz, *Principle of fluorescence spectroscopy*, 3rd ed, 1999.
- [28]. K. Zhang, Y. Yu, S. Sun, *Appl. Surf. Sci.*, 2013, 276, 333-339.
- [29]. R. Zhang, W. Chen, *Biosens. Bioelectron.*, 2014, 55, 83-90.
- [30]. L. Li, G. Wu, T. Hong, Z. Yin, D. Sun, E. S. Abdel-Halim, J. Zhu, *ACS Appl. Mater. Interfaces.*, 2014, 6, 2858-2864.
- [31]. Q. Lu, Y. Zhang, S. Lui, *J. Mater. Chem. A.*, 2015, 3, 8552-8558.
- [32]. Q. Lu, W. Wei, Z. Zhou, Z. Zhou, Y. Zhang, S. Liu, *Analyst*, 2014, 139, 2404-2410.

CHAPTER 5: Synthesis of B-doped graphene quantum dots as metal-free electrocatalyst for oxygen reduction reaction

5.1 Introduction

The electrochemical performance of fuel cells is largely limited by the sluggish reaction kinetics oxygen reduction reaction (ORR) [1, 2]. To date, platinum (Pt) and its alloys have been used as the most effective electrocatalyst for the ORR owing to high current density and a four-electron pathway. However, Pt-based electrocatalysts suffer from the limited resources, poor stability and deactivation by methanol and CO poisoning, which significantly impedes the commercial application of fuel cells. Thus, the various efforts have been devoted to explore non-precious metal or metal-free electrocatalysts for replacing Pt-based catalyst [3, 4]. Recently, metal-free carbon-based electrocatalysts have attracted a great deal of interest due to their excellent stability, low cost, good methanol and CO tolerance, compared to Pt-based catalysts. In particular, heteroatom-doped nanocarbon materials including carbon nanotubes, graphene and porous carbon exhibit good stability and electrocatalytic performance for the ORR [5, 6]. The introduction of heteroatoms (e.g. N, S and B) to nanocarbon materials is widely employed to modulate their intrinsic electrical and chemical characteristics by modifying the electronic structure of nanocarbons. Thus, heteroatom doped nanocarbon materials can be employed as promising materials in various applications [7-9]. The synthesis of B-doped nanocarbons could be an effective strategy for the metal-free electrocatalyst for ORR. Because B atoms incorporated with C atoms possess positive charge due to their lower electronegativity than C atoms, the adsorption of O₂ molecules on these B atoms easily occurs owing to the difference of electronegativity

between B and O atoms, causing the subsequent O₂ reduction. In this respect, the heteroatoms-doped graphene has been synthesized using graphene oxide (GO) or reduced graphene oxide (rGO) as starting materials for the energy-related applications [10, 11]. However, the synthesis of N-doped graphene and its properties have been extensively investigated. There have been only a few reports focusing on the synthesis and application of B-doped graphene, because of the difficulties in its synthesis, such as, the low doping level and high temperature process.

Similarly, the heteroatom-doped graphene quantum dots (GQD), zero-dimensional nanometer-sized graphene fragments with diameter around 5-20 nm, have attracted great attention for the practical efficiency toward metal-free ORR electrocatalyst. In particular, N-doped GQD have been extensively studied for the ORR electrocatalyst [12-14], and there are only a few studies demonstrating on the synthesis of B-doped GQD (BGQD) and their applications [15-19] due to the difficulty of synthesis. It still remains a challenge to develop a facile synthesis route of BGQD with low temperature process and high doping level. In this work, we have demonstrated that BGQD are synthesized by one-step and low temperature process and prepared the composites of rGO and BGQD (G-BGQD) for the application of metal-free electrocatalyst for ORR. Glucose and boric acid mixture as precursors were hydrothermally treated at 160°C, resulting in the production of BGQD with the uniform size and the controlled boron concentration. In addition, the resulting G-BGQD composites show the superior electrochemical performance for the ORR as metal-free electrocatalyst with better long-term durability and methanol tolerance than commercial Pt/C catalyst.

5.2 Experiment

5.2.1 Synthesis of BGQD

The various BGQD were synthesized by the carbonization of glucose (Sigma-Aldrich) with different concentration of boric acid (Sigma-Aldrich) through hydrothermal treatment as shown in Fig. 24a. To control the boron contents in GQD, 0.2, 0.4, and 0.6wt% of boric acid were used in this work. In brief, 4g of glucose was dissolved in 40 mL deionized water (DI), followed by adding 16 mg of boric acid (0.4wt%). After the mixture solution was stirred for 3 h at room temperature, it was then transferred into a 250 mL Teflon-lined stainless steel autoclave, and hydrothermally treated for 3h at 160°C. After cooling to room temperature, the light yellow solution was produced and the resulting solution was dialyzed using a dialysis tube (3000 Da, Spectrum Lab. Inc.) against DI for 2 days to remove unreacted chemicals and impurities. The BGQD solution was prepared with the concentration of 0.3 mg/mL. The synthesized BGQD with different boron contents were BGQD2, BGQD4 and BGQD6. Also, the undoped GQD was synthesized using the same procedure with no boric acid during the hydrothermal reaction.

5.2.2 Preparation of G-BGQD composites

Fig. 24b illustrates the preparation of G-BGQD composites by a simple hydrothermal process and thermal reduction. First, GO powder (Standard Graphene Co., GO-4401) was dissolves in DI water for 1 hour by ultrasonication to prepare the GO solution with the concentration of 0.5 mg/mL. Then, 40 mL of GO solution was mixed with 20 mL of BGQD solution (0.03mg/mL). After the mixture solution was stirred and sonicated for 1 hour, it was transferred into a 100 mL Teflon-lined stainless steel autoclave, and the hydrothermal treatment was carried out for 12 h at 180°C in the oven. After this procedure, GO sheets are partially reduced and their surface is decorated with BGQD due to the presence of strong π - π

stacking between GO and BGQD. The resulting sample was then freeze-dried to obtain the solid product. Finally, the solid product was placed in center of furnace tube and heated to 1000°C with heating rate of 5°C min⁻¹ under Ar atmosphere for the thermal reduction of GO, resulting in the enhancement of electrical conductivity of rGO.

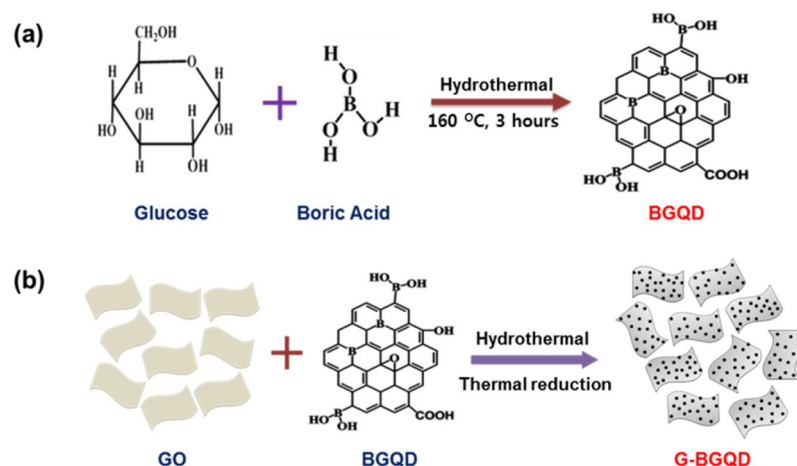


Fig. 24 Schematic illustration for the preparation of (a) BGQD and (b) G-BGQD composite materials

5.2.3 Characterizations

The nanostructures of samples were characterized by a transmission electron microscope (TEM, JEM-2100F, JEOL) with a 200 kV accelerating voltage and the surface morphologies and topographies of BGQD were observed by an atomic force microscope (AFM, Dimension 3100, Veeco) using non-contact mode with silicon cantilevers. Fourier transform infrared (FT-IR) spectra were obtained using a Nicolet IR 200 FT-IR spectrometer (Thermo Scientific). X-ray photoelectron-spectroscopy (XPS; Thermo Fisher) was performed using monochromatic AlK α radiation ($h\nu=1486.6$ eV). Electrical conductivity of G-BGQD composites was measured using a conventional four-probe system (Keithley 4200).

5.2.4 Electrochemical measurements

Cyclic voltammetry (CV) was performed to characterize the electrochemical performances on a multi-channel potentiostat-galvanostat analyser (VSP, Bio-logic) with a three-electrode system at room temperature. Pt wire and saturated calomel electrode (SCE) was used as counter and reference electrode, respectively. For the working electrode, the G-BGQD composites in ethanol (1 mg/mL) and 20 μ L Nafion in isopropyl alcohol solution (5 wt%) were mixed. Then, 5 μ l of this paste was loaded on a glassy-carbon electrode (GCE) dried in air. All the CV and rotating disk electrode (RDE) experiments using the modified glassy-carbon electrode was carried out in an O₂-saturated 0.1 M KOH electrolyte solution at room temperature. The number of electrons transferred per oxygen molecule in the ORR process was determined by the Koutecky-Levich (K-L) equation given below:

$$\frac{1}{j} = \frac{1}{j_k} + \frac{1}{B\omega^{0.5}}$$

Where j_k is the kinetic current density and ω is the electrode rotation rate. B could be determined from the slope of the K-L plots based on the following Levich equation:

$$B = 0.62 nF(D_{O_2})^{2/3} \nu^{-1/6} C_{O_2}$$

where n is the number of electrons transferred per oxygen molecule, F is the Faraday constant (96485 C mol⁻¹), D_{O_2} is the diffusion coefficient of O₂ in 0.1 M KOH (1.9×10⁻⁵ cm² s⁻¹), ν is the kinetic viscosity (1.0×10⁻² cm² s⁻¹) and C_{O_2} is the bulk concentration of O₂ in 0.1 M KOH (1.2×10⁻⁶ mol cm⁻³) [20, 21].

5.2.5 Computational method

All density functional theory (DFT) calculations were performed using DMol3 package [22, 23] in Accelrys's Materials Studio® version 8.0 software (Accelrys Software

Inc.). The Perdew-Burke-Ernzerhof (PBE) functional with generalized gradient approximation (GGA) was used [24, 25.] The double numerical basis sets with polarization function (DNP) were employed. The geometry optimization convergence tolerance for energy change was 10^{-5} Ha. The convergence tolerance for maximum force and the maximum displacement were $0.002 \text{ Ha}/\text{\AA}$ and 0.005\AA , respectively. Smearing of 0.003 Ha was applied and spin polarization was included in our studies. The van der Waals interactions were taken into account by the DFT-D3 correction [26]. The adsorption energy of molecular oxygen (O_2) was calculated by

$$E_{\text{ads}}(\text{eV}) = E_{\text{O}_2/\text{BGQD}} - E_{\text{O}_2} - E_{\text{BGQD}}$$

Where E_{ads} is the adsorption energy of O_2 on the BGQD surfaces. Also, $E_{\text{O}_2/\text{BGQD}}$, E_{O_2} and E_{BGQD} are the total surface energies of BGQD (BC_3 , BC_2O , or BCO_2 doped system) with the adsorbed O_2 , the total energy of gas phase O_2 , and the total surface energy of BGQD [27].

5.3 Results and discussion

Fig. 22a illustrates the preparation of BGQD through carbonization of glucose as carbon source with boric acid as boron source, based on the synthesis method reported from our group, which is a facile and environmentally friendly route using simple hydrothermal procedure at 160°C . Generally, the B-doping of graphene using GO or rGO as starting materials requires high temperature process [28, 29], whereas the proposed method in this work is carried out at low temperature due to the carbonization of glucose in the presence of boric acid.

Fig. 25a and b show the typical transmission electron microscopy (TEM) images of the synthesized BGQD. The prepared BGQD are well dispersed with relatively narrow size distribution and the average lateral size of 4 nm (Fig. 25c). Moreover, the lattice structure of BGQD was clearly found in the high resolution TEM (HRTEM) image of Fig. 1b with the lattice spacing distance of 0.24 nm, corresponding to the (1120) lattice of graphene, [29, 30] indicating the high crystallinity of the synthesized BGQD. Fourier transform infrared (FT-IR) spectroscopy of GQD and BGQD was performed to confirm the B-doping process. FT-IR spectra in Fig. 25d show that GQD and BGQD both have two stretching vibrations at 1387 and 3401 cm^{-1} corresponding to the peaks of -COO and -OH stretching modes which are typical peaks of the oxygen functional groups of graphene. However, the spectrum of BGQD exhibits an additional absorption peaks located at 1123 cm^{-1} assigned to B-C stretching, which suggests that the carbon atoms of graphene are successfully substituted by boron atoms.

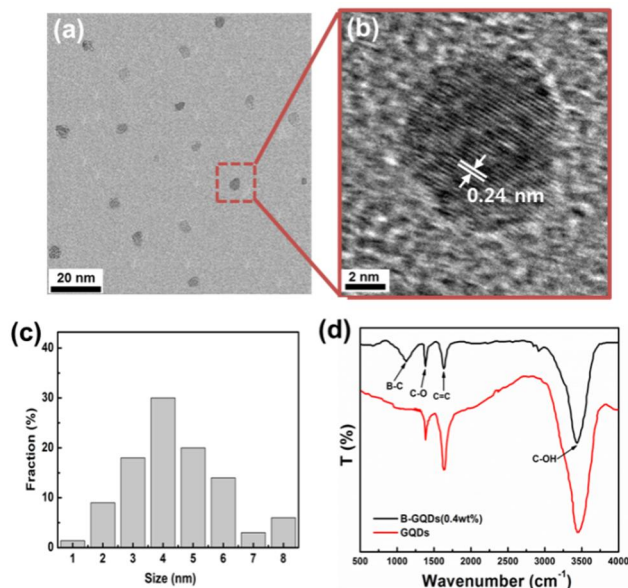


Fig. 25 (a) TEM and (b) HRTEM images of the as-synthesized BGQD and (c) the lateral size distribution of BGQD. (d) FT-IR spectrum of the undoped GQDs and BGQD.

The X-ray photoelectron spectroscopy (XPS) measurement was employed to probe the chemical composition and configuration of the BGQD. Fig. 26a shows the XPS survey scans for GQD and BGQD with different boric acid amount. The peaks of C1s and O1s are only observed in the survey scan of the undoped GQD, whereas the scans of all BGQD samples clearly exhibit C1s, O1s and B1s peaks centered at 284, 532, and 190 eV, respectively, indicating that the B atoms have been successfully introduced into the carbon lattice of GQD. The B1s peaks become more distinct as the increase of boric acid amount. The corresponding boron atomic percentages of BGQD2, BGQD4 and BGQD6 were derived from XPS elemental quantitative analysis and increase 2.34%, 3.65% and 4.25%, respectively. The high resolution C1s spectrum of BGQD4 can be fitted into five peaks as shown in Fig. 26c, corresponding to C-B (284 eV), sp^2 carbon C=C (284.6 eV), C-O bond (285.4 eV), C=O (286.6 eV) and O-C=O in carboxyl group (288 eV), while no C-B peak is observed for GQD as shown in Fig. 26b. The high resolution B 1s spectrum of BGQD4 can be fitted into four peaks, which is displayed in Fig. 26d. The peak at binding energy of 188.0 and 189.1 eV can be assigned to the BC_4 and BC_3 structures, respectively. Moreover, the peak at 190.3 eV is attributed to BC_2O structures and the peak at 191.2 eV corresponds to BCO_2 structures. The content of different B-C bond structures are calculated from the deconvoluted XPS spectra and summarized in Table 3. It can be seen that the highest composition of graphite-like BC_3 structure is attained for the BGQD4, while other BGQD samples have large portion of the oxidized B-C bond, such as BC_2O and BCO_2 structures. The BC_3 structures exhibit higher electronic conductivity and better O_2 chemisorption, compared to other BC_2O and BCO_2 structures, which is favorable for the electrocatalyst for the ORR [31-33].

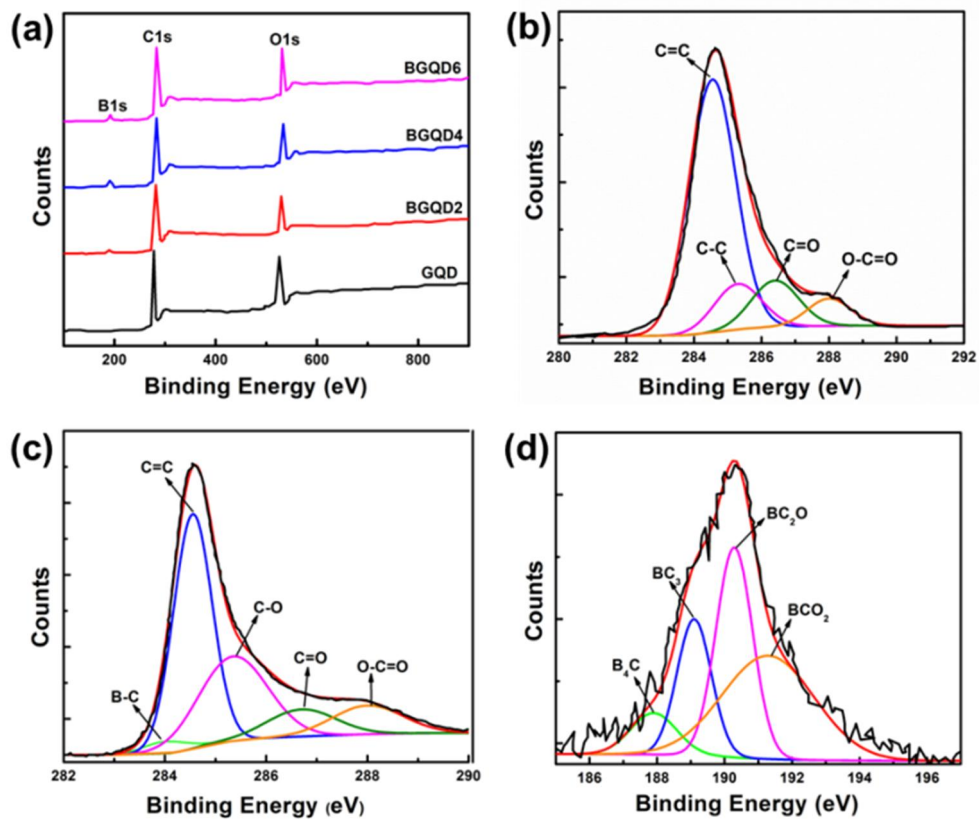


Fig. 26 (a) The XPS survey scan of GQD and BGQD with different boric acid concentration. High resolution C1s XPS spectra of (b) the undoped GQD and (c) BGQD4. (d) High resolution B1s XPS spectrum of BGQD4.

Table 3 Chemical composition of boron in different BGQD samples

Sample	B ₄ C (%)	BC ₃ (%)	BC ₂ O (%)	BCO ₂ (%)
BGQD2	0	10.85	15.50	73.64
BGQD4	11.46	42.33	30.58	15.63
BGQD6	10.26	20.23	43.87	25.64

The disadvantages of GQD for electrochemical applications are a poor electrical conductivity and their small size to form the network for an electron transport. In this regard, graphene sheets could act as excellent conductive pathway as well as carbon-based substrates for efficient electron transfer and uniform distribution of BGQD. We prepared the composites of G-BGQD to evaluate the electrocatalytic performance of BGQD. The simple hydrothermal process was carried out for the fabrication of composites of GO and BGQD, thus resulting in GO sheets decorated with BGQD due to the existence of strong π - π stacking force between them. SEM and TEM images of G-BGQD composite are shown in Fig. 27. After hydrothermal treatment and thermal reduction, a rough surface and slight porous structure of G-BGQD composite is formed as shown in Fig. 27a, which provides a sufficient surface area for the facile transport of electrolyte and electrons. TEM image in Fig. 27b clearly reveals that the BGQD are uniformly deposited on graphene sheets, indicating the successful preparation of G-BGQD composites.

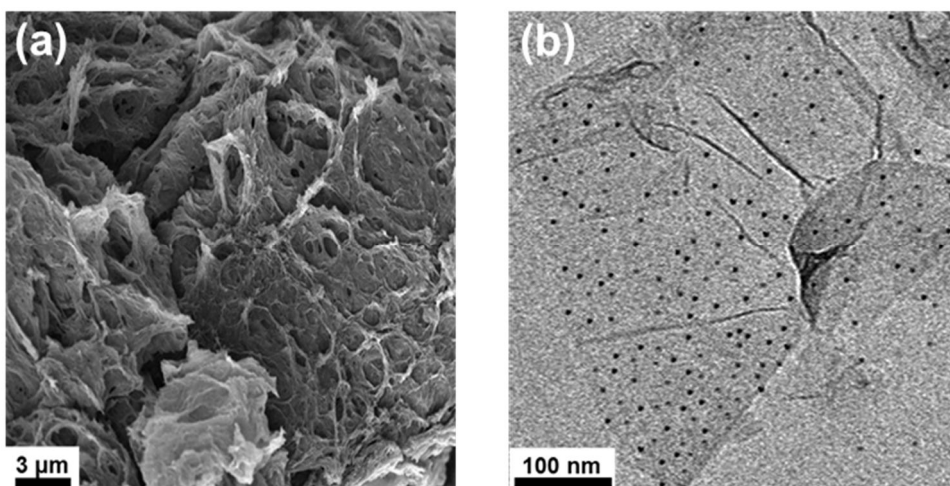


Fig. 27 (a) SEM and (b) TEM images of the prepared G-BGQD composite.

Fig.28a shows the CV curves for the G-BGQD composites in an O₂-saturated 0.1 M KOH electrolyte. It can be seen that the oxygen reduction peaks are observed for all G-BGQD composites. The reduction peak of the G-GQD composite is found at -0.37 V, and more positive reduction peaks with higher current density are found in the CV curves of G-BGQD composites. The most positive reduction peak of 0.27 V and highest peak current of -0.76 mA/cm² are measured for the G-BGQD4 composites. These results suggest that the composites with BGQD exhibit the enhanced electrocatalytic activity for ORR with faster oxygen reduction reaction than the undoped GQD.

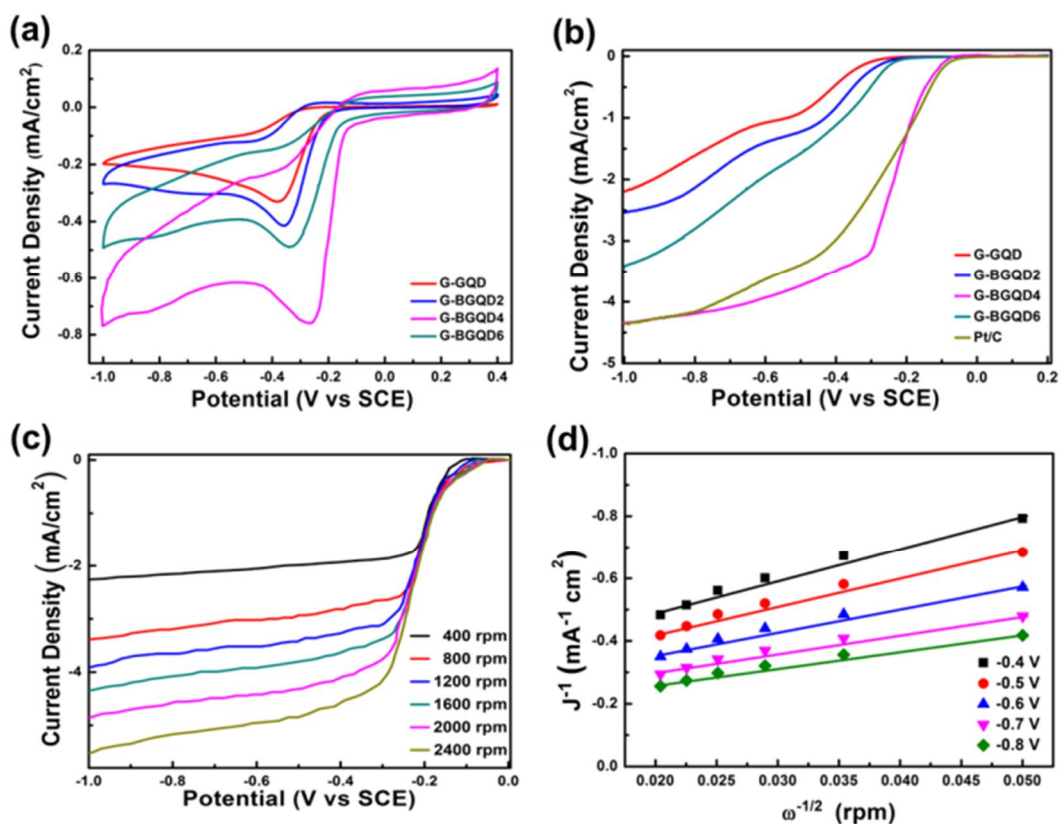


Fig. 28 (a) Cyclic voltammogram of different G-BGQD composites at a scan rate of 10 mV s^{-1} . (b) Linear sweep voltammetry (LSV) of different G-BGQD composites and commercial Pt/C catalyst. (c) LSV curves at different rotation speeds and (d) K-L plots at different potentials of G-BGQD4 composite.

Furthermore the electrocatalytic activity of G-BGQD composites toward the ORR was investigated by linear sweep voltammetry (LSV) using a rotating disk electrode (RDE). Fig. 28b shows the resulting LVS curves of G-GQD, G-BGQD composites and commercial Pt/C at a rotation speed of 1600 rpm in an O_2 -saturated 0.1 M KOH electrolyte. As the

important parameter for the electrocatalytic activity for ORR, the onset potential of oxygen reduction is evaluated. The onset potentials of oxygen reduction are determined from intersection of the tangents between the baseline and the signal current. The onset potentials of G-BGQD2, G-BGQD4 and G-BGQD6 composites are -0.31, -0.05 and -0.21 V, respectively. However, the onset potential of G-GQD composite is determined at -0.31 V. In addition to the onset potential, the higher limiting current density and positive shift of half-wave potentials of G-BGQD composites are also observed compared to that of G-GQD composite. Also, the G-BGQD4 composite shows the most positive onset potential and highest limiting current density, which is consistent with the above electrochemical performance results. When compared to the electrocatalytic activity of the commercial Pt/C catalyst, it is found that the ORR onset potential of -0.05 V and the limiting current density of 4.2 mA cm^{-2} for G-BGQD4, which are close to those of Pt/C (-0.08 V and 4.6 mA cm^{-2}). Moreover, the half-wave potential of G-BGQD4 is determined to be at -0.26 V which is close to that of the commercial Pt/C (-0.29 V).

Further RDE studies were performed at various rotation speeds to understand the ORR catalyzed by the composites. Fig. 28c shows the detailed RDE voltammetry of the G-BGQD4 composite at different rotation speeds. These data show that the increase of current densities is observed with an increase of rotation speed due to the shortened diffusion layer at higher speeds. Fig. 28d shows Koutecky-Levich (K-L) plots of G-BGQD4 at different potentials based on the RDE data of Fig. 28c. K-L plots reveal good linear relationship between the inverse of current density (j^{-1}) and the inverse of square root of the rotation rate ($\omega^{-1/2}$) over the potential from -0.4 to -0.8 V. Linearity of K-L plots of G-BGQD4 composite at different potentials suggests the first order kinetics toward ORR process. As the important

parameter for the kinetics of the ORR process, the electron transfer number (n) is calculated using the Levich equation from the slope of K-L plots. Among the various electrode materials, the electron transfer number (n) of G-BGQD4 is 3.81, which reveals that the ORR process of G-BGQD4 is a one-step, four-electron pathway. This superior electrocatalytic performance of G-BGQD is much higher than that of G-GQD ($n=2.24$) and comparable to that of the commercial Pt/C ($n=3.91$).

Based on the electrochemical analysis of G-BGQD composites, the superior electrocatalytic activity is demonstrated using the electrode with BGQD4 whose B-atomic concentration of 3.65% is lower than 4.25% of BGQD6. As shown in Table 3, compared with other B-C bond structures, the percentage of BC_3 increases with the increase of B-atomic concentration in BGQD, then it declines for BGQD6, which has the same tendency with the electrochemical performance of G-BGQD composites. The density functional theory (DFT) calculations were performed to investigate the electrocatalytic activity of various B-C bond structures in BGQD. The calculated adsorption energies of O_2 on various B-C bond structure of BGQD for different O_2 adsorption configurations. In previous work, we found that the O_2 adsorption was preferred to be on either top-top or bridge-bridge site of graphene, so we selected these adsorption sites as our initial sites for O_2 adsorption [34]. The calculated adsorption energies of O_2 on BC_3 structure were higher than those of BC_2O and BCO_2 structures in most O_2 adsorption configurations. For example, Fig. 29 shows the lowest energy configurations of O_2 adsorption on different B-C bond structures with the calculated adsorption energy: the calculated O_2 adsorption energy of BC_3 structure is -0.190 and -0.204 eV and those of BC_2O and BCO_2 structures are -0.162 and -0.133 eV, respectively. The configurations of an initial O_2 position in our calculations are constrained to the site near to

oxygen atom bonded to boron to consider the effect of BC_2O and BCO_2 structures for O_2 adsorption. Therefore, the adsorption of O_2 on BC_3 structure in BGQD is more favorable than BC_2O and BCO_2 structures. Other configurations and the calculated O_2 adsorption energies we examined at each case.

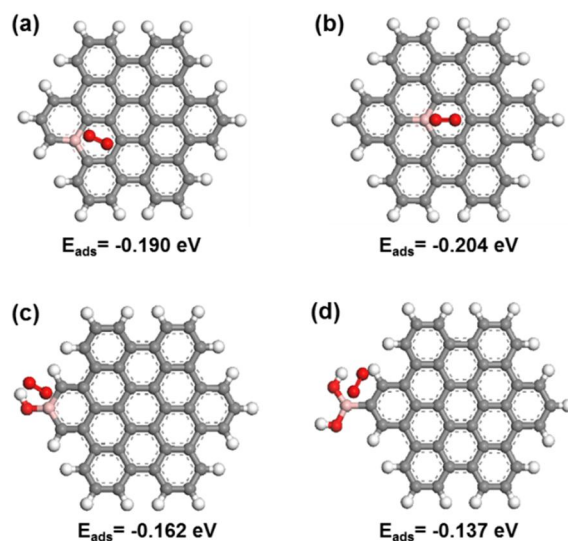


Fig. 29 Optimized structures of the lowest energy configurations of O_2 adsorption on different B-C bond structures in BGQD: (a-b) BC_3 , (c) BC_2O , and (d) BCO_2 bond structures. The gray, red and white colors denote carbon, oxygen and hydrogen, respectively.

Since the graphite-like BC_3 structures increase the hole-type charge carriers as well as the electron density of carbon atoms, the electric conductivity and electrocatalytic activity of BGQD are enhanced, compared to the BC_2O and BCO_2 structures by the oxidation of B-C bond in BGQD. The electrochemical impedance spectroscopy (EIS) was performed to explore the interface characteristics between catalyst and electrode. The Nyquist plots of G-BGQD composites with an equivalent circuit are shown in Fig. 30, where the R_s represents

the resistance of electrolyte solution, R_{ct} is charge-transfer resistance of catalyst and CPE is a constant phase element. The Nyquist plots of all G-BGQD composites exhibit the semicircles at high frequency region and the corresponding R_{ct} values are relatively low, indicating a good interfacial charge transfer between catalyst and electrode due to the π - π conjugation between rGO and BGQD. Obviously, the R_{ct} value of G-BGQD4 (9.2 Ω) is much lower than G-BGQD6 (14.3 Ω), indicating enhanced electronic conductivity in interface electrode. These results exhibit a good agreement with the above electrochemical characterizations, suggesting the proportion of graphite-like BC_3 structure in BGQD is the important parameter to enhance the electrocatalytic activity toward ORR.

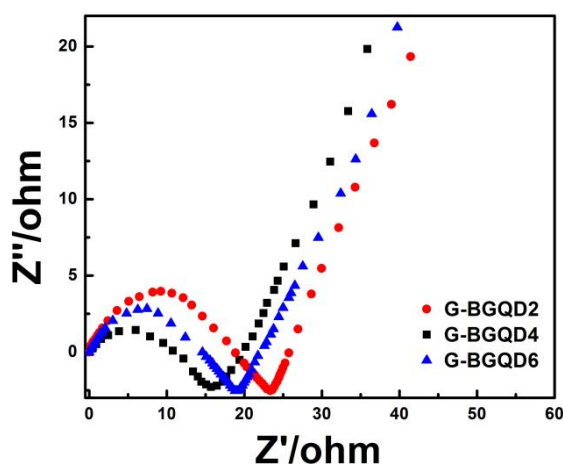


Figure 30 Nyquist plots of different G-BGQD composites.

Since fuel molecules such as methanol could cross over through the polymer membrane to cathode and seriously affect the whole cell performance, the methanol tolerance is important for the efficient electrocatalyst toward ORR application. The methanol tolerance of G-BGQD and commercial Pt/C catalyst is investigated as presented in Fig. 31a. After

adding 3.0 M methanol to the electrolyte, the chronoamperometric response for G-BGQD4 remains stable in an O₂-saturated 0.1 M KOH electrolyte, whereas the corresponding response for Pt/C catalyst instantaneously shows the significant drop due to the methanol oxidation reaction on Pt/C catalyst. In addition, the long-term stability of G-BGQD composite was evaluated by carrying out chronoamperometric responses in an O₂-saturated solution at 0.8 V with a rotation rate of 1600 rpm. As shown in Fig. 31b, a slight current density loss is observed for G-BGQD4 composite after 25 hours test, whereas the corresponding current density loss for Pt/C catalyst exhibits is much higher up to 63%. These results clearly indicate that the G-BGQD composite possesses a better electrocatalytic performance in the tolerance for methanol crossover and in the long-term stability, compared with the commercial Pt/C catalyst.

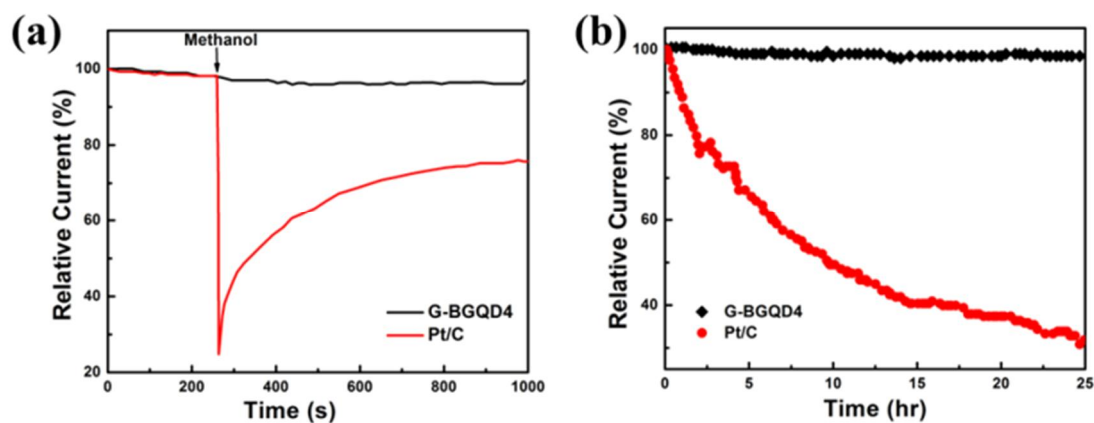


Fig. 31 Chronoamperometric response of G-BGQD4 and Pt/C on addition of 3 M methanol added after 250 s at -0.8 V (vs SCE) and a rotation speed of 1600 rpm. (b) Chronoamperometric curves of G-BGQD4 and Pt/C at -0.8 V and a rotation speed of 1600 rpm.

5.4 Conclusion

In summary, we have successfully prepared BGQD by a facile and environment friendly method at low temperature through one-step hydrothermal treatment of glucose with boric acid. The synthesized BGQD reveals uniform nm-size distribution and high B-doping level up to 4.25%, and enhanced excellent electrocatalytic activity, compared to the undoped GQD. We also prepared G-BGQD composites for the practical ORR electrocatalyst application. The G-BGQD composites exhibit the excellent electrocatalytic activity toward ORR including comparable onset potential and limiting current density with Pt/C catalyst as well as one-step, four-electron pathway for ORR. Moreover, the G-BGQD composite displays higher long-term stability and tolerance to methanol crossover than those of the commercial Pt/C catalyst. In G-BGQD composite, BGQD provide abundance of active site for catalyzing the reduction of oxygen, and rGO act as highly conductive pathway to transfer electron from BGQD into electrode. Based on these results, the G-BGQD can be a greatly promising electrocatalyst candidate for a new class of efficient and cost effective metal-free catalyst for ORR in fuel cells and other electrochemical applications.

Reference

- [1]. M. Winter and R. J. Brodd, *Chem. Rev.*, 2004, 104, 4245–70.
- [2]. M. K. Debe, *Nature*, 2012, 486, 43-51.
- [3]. H. A. Gasteiger and N. M. Markovic, *Science*, 2009, 324, 48-9.
- [4]. Morozan, B. Joussetme and S. Palacin, *Energy Environ. Sci.*, 2011, 4, 1238-54.
- [5]. L. Dai, Y. Xue, L. Qu, H. J. Choi and J. B. Baek, *Chem. Rev.*, 2015, 115, 4823–92.
- [6]. M. Zhang and L. Dai, *Nano Energy*, 2012, 1, 514–7.
- [7]. Z. Zhang, T. Zheng, X. Li, J. Xu and H. Zeng, *Part. Part. Syst. Charact.*, 2016, 33, 457-472.
- [8]. W. J. Ong, L. K. Putri, Y. C. Tan, L. L. Tan, N. Li, Y. H. Ng, X. Wen and S. P. Chai, *Nano Res*, 2017, DOI:10.1007/s12274-016-1391-4.
- [9]. S. HU, *Chem. Rec.*, 2016, 16, 219-230.
- [10]. L. K. Putri, B. J. Ng, W. J. Ong, H. W. Lee, W. S. Chang and S. P. Chai, *ACS Appl. Mater. Interfaces*, 2017, 9, 4558-4569
- [11]. R. Ma, X. Ren, B. Y. Xia, Y. Zhou, C. Sun, Q. Lui, J. Lui and J. Wang, *Nano Res.*, 2016, 9, 808-819.
- [12]. Y. Du and S. Guo, *Nanoscale*, 2016, 8, 2532-43.
- [13]. X. Li, M. Rui, J. Song, Z. Shen and H. Zeng, *Adv. Funct. Mater.*, 2015, 25, 4929-47.
- [14]. Q. Li, S. Zhang, L. Dai and L.-s. Li, *J. Am. Chem. Soc.*, 2012, 134, 18932–5.

- [15]. M. Favaro, F. Carraro, M. Cattelan, L. Colazzo, C. Durante, M. Sambì, A. Gennaro, S. Agnoli and G. Granozzi, *J. Mater. Chem. A*, 2015, 3, 14334–47.
- [16]. H. Fei, R. Ye, G. Ye, Y. Gong, Z. Peng, X. Fan, E. L. G. Samuel, P. M. Ajayan and J. M. Tour, *ACS Nano*, 2014, 8, 10837-43.
- [17]. M. Favaro, L. Ferrighi, G. Fazio, L. Colazzo, C. D. Valentin, C. Durante, F. Sedona, A. Gennaro, S. Agnoli and G. Granozzi, *ACS Catal.*, 2015, 5, 129-44.
- [18]. L. Zhang, Z. Y. Zhang, R. P. Liang, Y. H. Li, and J. D. Qiu, *Anal. Chem.*, 2014, 86, 4423-30.
- [19]. C. Dou, S. Saito, K. Matsuo, I. Hisaki, and S. Yamaguchi, *Angew. Chem. Int. Ed.*, 2012, 51, 12206-10.
- [20]. N. B. Trung, T. V. Tam, H. R. Kim, S. H. Hur, E. J. Kim and W. M. Choi, *ChemEng J.*, 2014, 25, 589-96.
- [21]. R. Liu, D. Wu, X. Feng and K. Müllen, *Angew. Chem. Int. Ed.*, 2010, 49, 2565-9.
- [22]. B. Delley, *J. Chem. Phys.*, 2000, 113, 7756.
- [23]. B. Delley, *Comp. Mater. Sci.*, 2000, 17, 122-126.
- [24]. J. P. Perdew, K. Burke, and M. Ernzerhof, *Phys. Rev. Lett.*, 1996, 77, 3865-8.
- [25]. J. P. Perdew, K. Burke, and Y. Wang, *Phys. Rev. B*, 1996, 54, 16533.
- [26]. S. Grimme, J. Antony, S. Ehrlich, and H. Krieg, *J. Chem. Phys.*, 2010, 132, 154104.
- [27]. D. Sholl and J. A. Steckel, *Density Functional Theory: A Practical Introduction*, John Wiley & Sons, Inc., New Jersey, 2009

- [28]. J. Han, L. L. Zhang, S. Lee, J. Oh, K.-S. Lee, J. R. Potts, J. Ji, X. Zhao, R. S. Ruoff and S. Park, *ACS Nano*, 2013, 7, 19–26.
- [29]. J. Peng, W. Gao, B. K. Gupta, Z. Liu, R. Romero-Aburto, L. Ge, L. Song, L. B. Alemany, X. Zhan, G. Gao, S. A. Vithayathil, B. A. Kaiparettu, A. A. Marti, T. Hayashi, J. J. Zhu and P. M. Ajayan, *Nano Lett.*, 2012, 12, 844–9.
- [30]. G. Eda, Y. Y Lin, C. Mattevi, H. Yamaguchi, H. A. Chen, I. S. Chen, C. W. Chen and M. Chhowalla, *Adv. Mater.*, 2010, 22, 505-9.
- [31]. C. Wang, Z. Guo, W. Shen, Q. Xu, H. Liu and Y. Wang, *Adv. Funct. Mater.*, 2014, 24, 5511-21.
- [32]. Y. A. Kim, K. Fujisawa, H. Muramatsu, T. Hayashi, M. Endo, T. Fujimori, K. Kaneko, M. Terrones, J. Behrends, A. Eckmann, C. Casiraghi, K. S. Novoselov, R. Saito and M. S. Dresselhaus, *ACS Nano*, 2012, 6, 6293–6300.
- [33]. L. Yang, S. Jiang, Y. Zhao, L. Zhu, S. Chen, X. Wang, Q. Wu, J. Ma, Y. Ma and Z. Hu, *Angew. Chem., Int. Ed.*, 2011, 50, 7132–7135.
- [34]. J. H. Lee, S. G. Kang, H. S. Moon, H. Park, I. T. Kim, and S. G. Lee, *Appl. Surf. Sci.*, 2015, 351, 193-202.

CHAPTER 6: CONCLUSION

Graphene quantum dots are potentially abundantly available and at the same time have optoelectronic properties that make them an interesting advanced material for many applications. It has been demonstrated that GQDs can be used in diverse areas spanning from energy harvesting and storage to bio analytics. Despite this great potential, the main difficulty is still the production of high-quality GQDs. In this studies, many methods has been developed for the large-scale synthesis of GQDs of well-defined size and chemical functionality is still lacking and would certainly boost research and applications in this area.